

Observation of undepleted phosphine in the atmosphere of a low-temperature brown dwarf

Adam J. Burgasser^{1*}, Eileen C. Gonzales², Samuel A. Beiler³, Channon Visscher^{4,5}, Ben Burningham⁶, Gregory N. Mace⁷, Jacqueline K. Faherty⁸, Zenghua Zhang^{9,10}, Clara Sousa-Silva^{11,12}, Nicolas Lodieu^{13,14}, Stanimir A. Metchev¹⁵, Aaron Meisner¹⁶, Michael Cushing³, Adam C. Schneider¹⁷, Genaro Suarez⁸, Chih-Chun Hsu¹⁸, Roman Gerasimov¹⁹, Christian Aganze²⁰, Christopher A. Theissen¹

¹Department of Astronomy & Astrophysics, University of California, San Diego, La Jolla, CA, USA

²Department of Physics and Astronomy, San Francisco State University, San Francisco, CA, USA

³Ritter Astrophysical Research Center, Department of Physics & Astronomy, University of Toledo, Toledo, OH, USA

⁴Chemistry & Planetary Sciences, Dordt University, Sioux Center, IA, USA

⁵Center for Exoplanetary Systems, Space Science Institute, Boulder, CO, USA

⁶Centre for Astrophysics Research, Department of Physics, Astronomy and Mathematics, University of Hertfordshire, Hatfield, UK

⁷Department of Astronomy, University of Texas at Austin, Austin, TX, USA

⁸Department of Astrophysics, American Museum of Natural History, New York, NY, USA

⁹School of Astronomy and Space Science, Nanjing University, Nanjing, China

¹⁰Key Laboratory of Modern Astronomy and Astrophysics, Nanjing University, Ministry of Education, Nanjing, China

¹¹Bard College, Annandale-on-Hudson, NY, USA

¹²Institute of Astrophysics and Space Sciences, Porto, Portugal

¹³Instituto de Astrofísica de Canarias, La Laguna, Tenerife, Spain

¹⁴Departamento de Astrofísica, Universidad de La Laguna, La Laguna, Tenerife, Spain

¹⁵Department of Physics & Astronomy, Western University and Institute for Earth and Space Exploration, London, ON, Canada

¹⁶National Science Foundation's National Optical-Infrared Astronomy Research Laboratory, Tucson, AZ, USA

¹⁷United States Naval Observatory, Flagstaff Station, Flagstaff, AZ, USA

¹⁸Center for Interdisciplinary Exploration and Research in Astrophysics, Northwestern University, Evanston, IL, USA

¹⁹Department of Physics and Astronomy, University of Notre Dame, Notre Dame, IN, USA

²⁰Kavli Institute for Particle Astrophysics & Cosmology, Stanford University, Stanford, CA, USA

*Corresponding author. Email: aburgasser@ucsd.edu

The atmospheres of low-temperature brown dwarfs and gas giant planets are expected to contain the phosphine molecule, PH₃. However, previous observations have shown much lower abundances of this molecule than predicted by atmospheric chemistry models. We report JWST spectroscopic observations of phosphine in the atmosphere of the brown dwarf Wolf 1130C. Multiple absorption lines due to phosphine are detected around 4.3 μ m, from which we calculate a phosphine abundance of 0.100 ± 0.009 parts per million. This abundance is consistent with disequilibrium atmospheric chemistry models that reproduce the phosphine abundances in Jupiter and Saturn, and is much higher than abundances previously reported for other brown dwarfs or exoplanets. This difference may be related to the low abundance of heavy elements in Wolf 1130C.

Phosphorus and phosphorous molecules have been observed in the atmospheres of Saturn (1) and Jupiter (2), in the interstellar medium (3), and in the circumstellar material around evolved stars (4). The molecular hydride phosphine (PH₃) has been proposed as a potential biosignature for exoplanet atmospheres (5). Phosphorus is primarily synthesized in the interiors of massive stars through the slow neutron capture process (6) and released into the interstellar medium when they explode as supernovae. The abundance of phosphorus within the Milky Way therefore traces the history of massive stars over the lifetime of the Galaxy (7, 8).

In the Sun, phosphorus has an abundance of about 0.3 parts per million (ppm) measured relative to hydrogen, the most abundant element (9). Spectroscopic studies of bright giant stars at ultraviolet (10) and infrared wavelengths (8, 11) have shown that phosphorus can be 2 to 3 times more abundant than predicted by Milky Way evolution models (7, 12). A distinct class of phosphorus-rich (P-rich) stars have also been identified, with abundances ten times the solar value (13). These P-rich stars are ancient giant stars with low atmospheric metallicity (low abundances of elements heavier than helium). Their origin is unclear; they might indicate that our understanding of phosphorus production through neutron capture processes is incomplete (14) or that there are additional sites of phosphorus synthesis (15).

Phosphine has been predicted to be the primary phosphorous molecule in the low-temperature atmospheres of brown dwarfs and gas giant exoplanets (16, 17). The abundances of PH₃ in the atmospheres of Jupiter and Saturn are 2 to 6 ppm, implying that phosphorus in those planets is enriched by factors of 5 to 16 compared to the Sun (18–20). However, observational searches for PH₃ in brown dwarf (21–24) and exoplanet atmospheres (25–27) have provided only upper limits that are 100 times lower than the abundances predicted by atmosphere models (24). PH₃ has been detected in the atmosphere of the low-temperature brown dwarf WISE 0855–0714 with an abundance of 1 part per billion (ppb), 200 times lower than predicted by models, even accounting for this object's low metallicity (28). Observational searches for PH₃ in the infrared spectra of cool atmospheres are hampered by a strong absorption band of CO₂ which overlaps with the 4.3 μ m band of PH₃. In contrast to PH₃, CO₂ is up to 5,000 times more abundant than predicted from atmosphere models (24). These discrepancies indicate that our understanding of phosphorus chemistry and chemical dynamics in cool atmospheres is incomplete.

The Wolf 1130ABC system

The Wolf 1130ABC system (= HIP 98905 = LHS 482 = GJ 781AB) is a triple star system 17 parsecs (pc) from the Sun, composed of a low mass star (Wolf 1130A = GJ 781A) and white dwarf (Wolf 1130B) in a short-period (0.5 day) binary orbit, with a cold (≈ 600 K), widely-separated ($\sim 3,000$ astronomical units) brown dwarf tertiary, Wolf 1130C (= GJ 781B = WISE J200520.38+542433.9; (29–31)). Wolf 1130A has an iron abundance five times lower than the Sun (logarithmic measure of $[\text{Fe}/\text{H}] = -0.70 \pm 0.12$) and is enriched in elements associated with massive star nucleosynthesis (31, 32). These abundance patterns, and the high velocity of the system relative to the Sun, indicate that it is part of the Milky Way’s thick disk, which consists of old stars (33). Previous spectral observations of Wolf 1130C have shown that it also has a low metallicity atmosphere (30, 34), and our observations confirm that the source has a low bolometric luminosity, $\log_{10} (L_{\text{bol}}/L_{\odot}) = -6.047 \pm 0.003$, consistent with a low-temperature brown dwarf (35).

Observation of Phosphine in Wolf 1130C

We observed Wolf 1130C using the Near-Infrared Spectrograph (NIRSpec (36)) and the Mid-Infrared Imager (MIRI (37)) on JWST on 2024 Aug 30 (35). With NIRSpec, we used the Prism mode with the combined S200A1 0''.2-wide slit to obtain low-resolution spectra (resolving power $\lambda/\Delta\lambda \approx 100$) spanning the wavelength range 0.6 to 5.2 μm , and the G395H grating mode with the S200A1 and S200A2 0''.2-wide slits to obtain moderate-resolution spectra ($\lambda/\Delta\lambda \approx 3,000$) spanning 3.8 to 5.2 μm . With MIRI, we used the Low Resolution Spectroscopy (LRS) mode with the 0''.51-wide slit to obtain low-resolution spectra ($\lambda/\Delta\lambda \approx 100$) spanning 4 to 14 μm . For the NIRSpec/Prism observations, four exposures totaling 997 s were obtained, resulting in a median signal-to-noise (S/N) of 300 at 4.1 μm . For the NIRSpec/G395H observations, four exposures totaling 1099 s were obtained, resulting in a median S/N of 75 at 4.1 μm . For the MIRI/LRS observations, two exposures totaling 555 s were obtained, resulting in a median S/N of 90 at 9 μm .

Fig. 1A shows the NIRSpec/Prism spectrum of Wolf 1130C, compared to that of the brown dwarf ULAS J102940.52+093514.6 (hereafter ULAS J1029+0935), which has a similar effective temperature ($T_{\text{eff}} \approx 700$ K (38)) but kinematics consistent with the Milky Way’s thin disk population (39). The spectra of both sources have similar molecular absorption features, which are common to low-temperature brown dwarfs, but they are clearly distinct in the 1.5 to 2.5 μm region where Wolf 1130C is fainter and the 3 to 5 μm region where Wolf 1130C is brighter than ULAS J1029+0935.

The spectrum of Wolf 1130C has an additional absorption feature centered at 4.3 μm (Fig. 1A–B). We identify this feature as the blended ν_1 and ν_3 fundamental vibrational bands of PH_3 , where the subscript indicates the vibrational quantum number. Those bands are split into P-, Q-, and R-branch rotational lines, with the main feature at 4.3 μm being the blended Q-branch lines. In the higher-resolution spectrum (Fig. 1D), we also identify individual P- and R-branch lines in the 4.1 to 4.2 μm and 4.35 to 4.45 μm regions respectively, interspersed with lines of CH_4 and H_2O . In contrast, the spectrum of ULAS J1029+0935 shows strong CO_2 absorption in this region (Fig. 1C), which is absent in the spectrum of Wolf 1130C.

Atmospheric Chemistry Modeling

We compare the NIRSpec/Prism spectrum of Wolf 1130C to previously-published low-temperature atmospheric models (24, 40) in Fig. 2 (35). We find that the observed PH₃ absorption bands can be reproduced by models that include disequilibrium chemistry driven by vertical mixing of gas within the upper atmosphere. This process is responsible for the PH₃ enrichment observed in the atmospheres of Jupiter and Saturn (41, 42). Theoretical studies have predicted that vertical mixing affects the abundances of other molecules in low-temperature atmospheres, including CH₄, CO, CO₂, and NH₃ (43, 44). We examined modifications to the predicted atmospheric abundances of PH₃ and CO₂ relative to disequilibrium chemistry models, accounting for the overall reduction of C and O elemental abundances of Wolf 1130A relative to the Sun (24). We find that the line strengths of both absorption features are consistent with model predictions (35), in contrast to other brown dwarfs which show reduced abundances of PH₃ and enhanced abundances of CO₂ relative to disequilibrium chemistry models (24, 40).

We performed an abundance analysis of Wolf 1130C using the NIRSpec/G395H spectrum and the BREWSTER atmospheric retrieval framework (35, 45, 46). Fig. 3A shows the retrieved spectral model, which reproduces the G395H spectrum. Fig. 3B compares the retrieved abundances of H₂O, CH₄, CO, CO₂, NH₃, H₂S, and PH₃ to predictions of chemical equilibrium models for the metallicity and C/O ratio of the Wolf 1130 system (17, 47). The retrieval finds abundances of H₂O, CH₄, and H₂S that are consistent with the predictions of equilibrium chemistry models, while abundances of CO and PH₃ are consistent with vertical mixing of gas from deep below the photosphere. Our retrieved PH₃ abundance of 0.100 ± 0.009 ppm is 100 times larger than the PH₃ abundance measured for WISE J0855–0714 (28). Absorption features from CO₂ are only marginally detected, so its abundance is poorly constrained but likely less than 0.6 ppb.

From the retrieved molecular abundances, we infer that Wolf 1130C has a low metallicity, with a logarithmic metal abundance of $[M/H] = -0.68 \pm 0.04$ ($20.9\% \pm 1.9\%$) relative to the Sun; and a carbon/oxygen abundance ratio 0.26 ± 0.01 , also significantly less than the Sun. These values are consistent with the composition of Wolf 1130A (31) and other stars in the Milky Way’s thick disk population (48). Assuming these molecules contain the bulk of C, O, P, and S in the photosphere of Wolf 1130C, we calculate that it is enriched relative to the Sun in phosphorus (1.7 ± 0.2 times larger) and oxygen (2.1 ± 0.3 times larger), but has a solar metal abundance fraction of carbon and sulfur. These elemental abundance patterns match those of other metal-poor stars in the thick disk population (48).

Implications of Phosphine Detection

The presence of strong phosphine absorption in the spectrum of Wolf 1130C is unlike other observed low-temperature brown dwarf and giant exoplanet spectra, which are highly depleted in PH₃ relative to vertical mixing models (24, 28). The higher abundance of PH₃ in the atmosphere of Wolf 1130C may be due to its low metallicity. All other effects being equal, reducing the elemental abundances of carbon and oxygen by a factor of ten reduces the CO₂ abundance by a factor of one thousand (Fig. S6), which in turn reduces the strength of the prominent 4.3 μ m CO₂ ν_2 absorption band. Removal of this band may explain why the weaker 4.3 μ m PH₃ feature can be observed in Wolf 1130C (Fig. 1).

However, lower CO₂ opacity does not explain why the overall abundance of PH₃ in Wolf 1130C is consistent with vertical mixing models, while this molecule is highly depleted in other brown dwarfs and gas giant exoplanets. Our chemical equilibrium models (Fig. 4) show that the formation of NH₄H₂PO₄, a condensate that removes PH₃ gas from low-temperature atmospheres, occurs at a lower temperature and pressure in a more metal-poor atmosphere (35). This shift in the condensation curve allows PH₃ to exist over a wider portion of the photosphere compared to metal-enriched atmospheres. However, both Jupiter and Saturn have metal-enriched atmospheres and are considerably colder than Wolf 1130C (T_{eff} ≈ 100 K compared to ≈ 600 K), which is inconsistent with delayed condensation as an explanation. We also consider the role of intermediate phosphorus oxides in the depletion of PH₃ (35), including P₄O₆ which has poorly constrained thermodynamic properties (49). We find that varying the chemical properties of P₄O₆ reduces PH₃ equilibrium abundances, matching those of other brown dwarfs and giant exoplanets, but fails to explain the higher abundances in Wolf 1130C, Jupiter, and Saturn.

Wolf 1130C's high PH₃ abundance could alternatively be due to modest enrichment of elemental phosphorus inferred from our retrieval analysis. Previous studies of metal-poor stars have found phosphorus is enriched to levels exceeding the predictions of Galactic nucleosynthesis models (7, 12), by up to an order of magnitude (13). One possibility is that the massive white dwarf component of this system, Wolf 1130B, could be a local source of phosphorus enhancement. The 6 to 8 solar mass progenitor of this component can produce phosphorus through slow neutron capture nucleosynthesis during a late giant phase of its evolution (50), and enrich Wolf 1130C during the planetary nebular stage. The current 1.2 M_⊕ white dwarf remnant could in principle also produce phosphorus through proton capture nucleosynthesis of material deposited onto its surface by its close companion Wolf 1130A, and subsequently ejected during novae episodes (15, 51). However, the spectrum of Wolf 1130A shows no evidence of phosphorus enrichment (35). We therefore suggest that the slightly elevated abundance of phosphorus in Wolf 1130C is more likely to reflect the composition of metal-poor stars in the Milky Way's thick disk, rather than local production.

We conclude that phosphine is present in Wolf 1130C at an abundance consistent with vertical mixing processes, similar to Jupiter and Saturn but unlike other brown dwarf and gas giant atmospheres. The inability of models to consistently explain all these sources indicates an incomplete understanding of phosphorus chemistry in low-temperature atmospheres. We therefore caution against the use of phosphine as a biosignature until these discrepant findings are resolved.

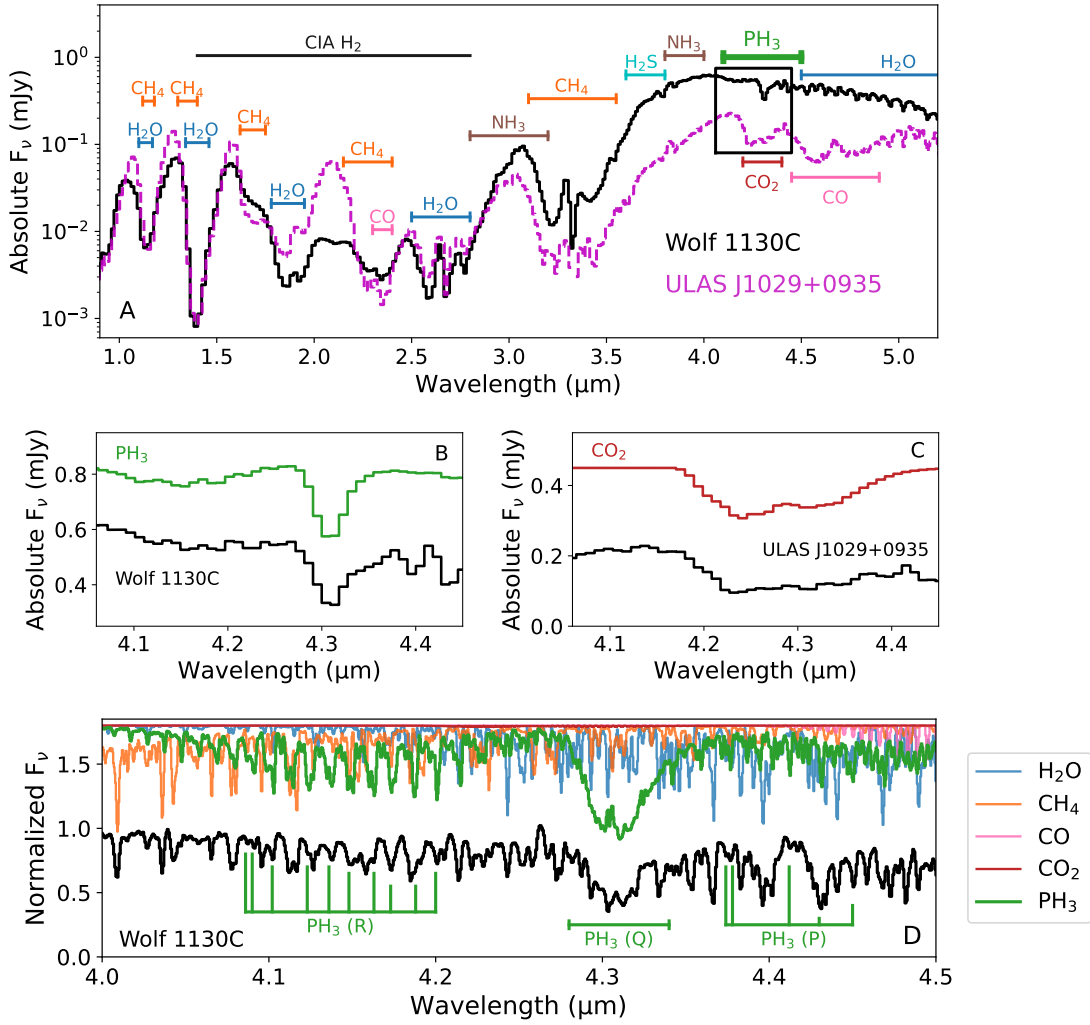


Figure 1: JWST NIRSpec spectra of Wolf 1130C compared to ULAS J1029+0935 and models. (A) The 0.9 to 5.2 μm NIRSpec/Prism spectra of Wolf 1130C (black solid line) and the brown dwarf ULAS J1029+0935 (magenta dashed line) (38) in absolute F_ν flux densities (flux per unit frequency) measured in milliJanskies (mJy). Colored bars indicate identified molecular absorption features in this region, as labeled. We also indicate the 1.4 to 2.8 μm region where collision-induced absorption (CIA) from H_2 influences low-temperature spectra (horizontal black line). The box centered at 4.25 μm highlights the region shown in panels B and C. (B) 4.05 to 4.45 μm region of the spectrum of Wolf 1130C (black line) compared to a theoretical absorption spectrum of PH_3 at an equivalent temperature (green line). (C) Same as panel (B) but comparing the spectrum of ULAS J1029+0935 (black line) to a theoretical absorption spectrum of CO_2 (red line). (D) Normalized NIRSpec/G395H spectrum of Wolf 1130C in the 4.0 to 4.5 μm region (black line) compared to theoretical absorption spectra for H_2O (blue), CH_4 (orange), CO (pink), CO_2 (red), and PH_3 (green) at the temperature and relative abundances inferred from our retrieval analysis (Table S2). Green lines and labels indicate the identified blended Q-branch and individual R- and P-branch lines of PH_3 .

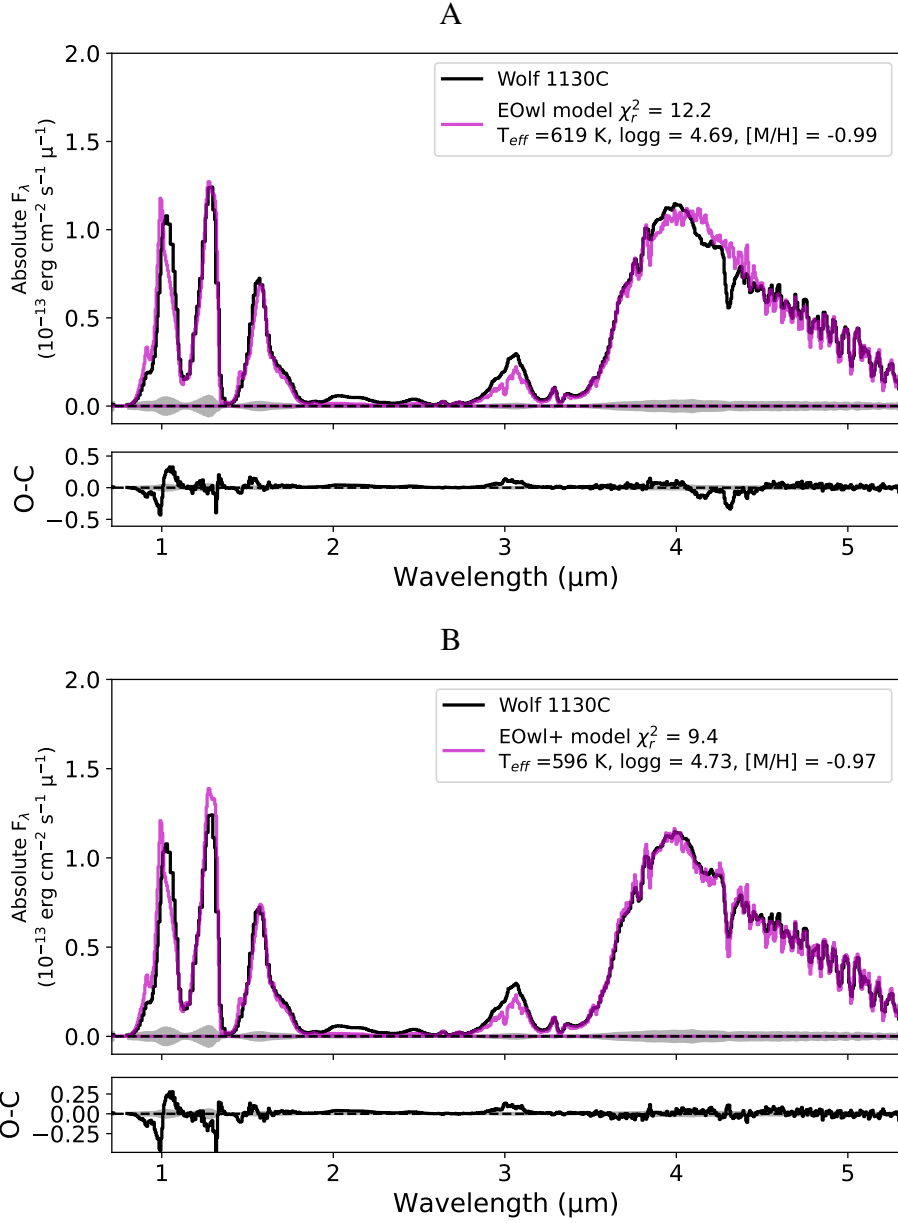


Figure 2: Sonora Elf-Owl models fitted to the spectrum of Wolf 1130C. (A) The observed spectrum fitted by models with artificially suppressed PH_3 abundances (EOwl (40)); (B) the same but using models with PH_3 abundances set by vertical mixing (EOwl+ (24)). Both figures compare the absolute flux-calibrated spectrum (black lines) to the best-fitting model (magenta line) and 20 draws from the MCMC posterior chains (pale magenta lines) as an indication of the model uncertainty. Below each panel we show the difference (observed minus computed, or O-C) between the observed and best-fitting model spectra and the $\pm 5\sigma$ uncertainty of the former (grey bands). The dashed black lines indicate zero flux.

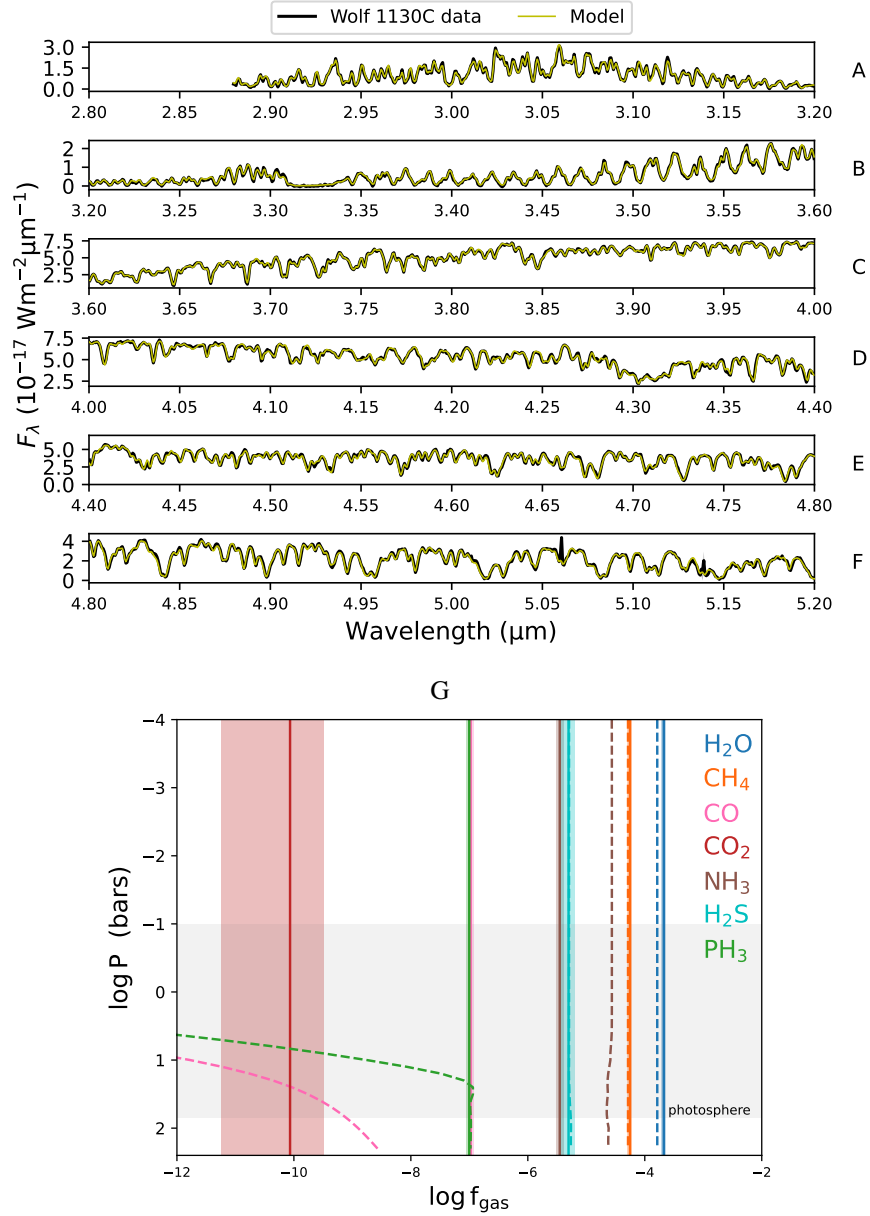


Figure 3: Retrieval analysis of the NIRSpec/G395H spectrum of Wolf 1130C. (A-F) The G395H spectrum (black line) compared to the median likelihood atmosphere model from our retrieval analysis (mustard line). The two are nearly indistinguishable, with a reduced $\chi^2 = 6$. Single pixel deviations at 5.06 μm and 5.14 μm are due to noise. (G) Retrieved abundances (solid vertical lines) for H_2O (blue), CH_4 (orange), CO (pink), CO_2 (red), NH_3 (brown), H_2S (cyan), and PH_3 (green) plotted as a function of logarithmic pressure ($\log P$) in the photosphere. Shaded regions around each line indicate the $\pm 1\sigma$ uncertainties on the retrieved abundances from the retrieval posterior distributions (Fig. S3). Dashed lines are the predicted abundances for a $[\text{M}/\text{H}] = -0.7$, $\text{C}/\text{O} = 0.26$ thermochemical equilibrium model. CO_2 is not visible in this plot as its equilibrium abundance is $< 10^{-12}$ (Fig. S6). Grey shading indicates the approximate pressure region of the photosphere (visible layer of the atmosphere) in the 3 to 5 μm region. The retrieved abundances are assumed to be constant at all pressures.

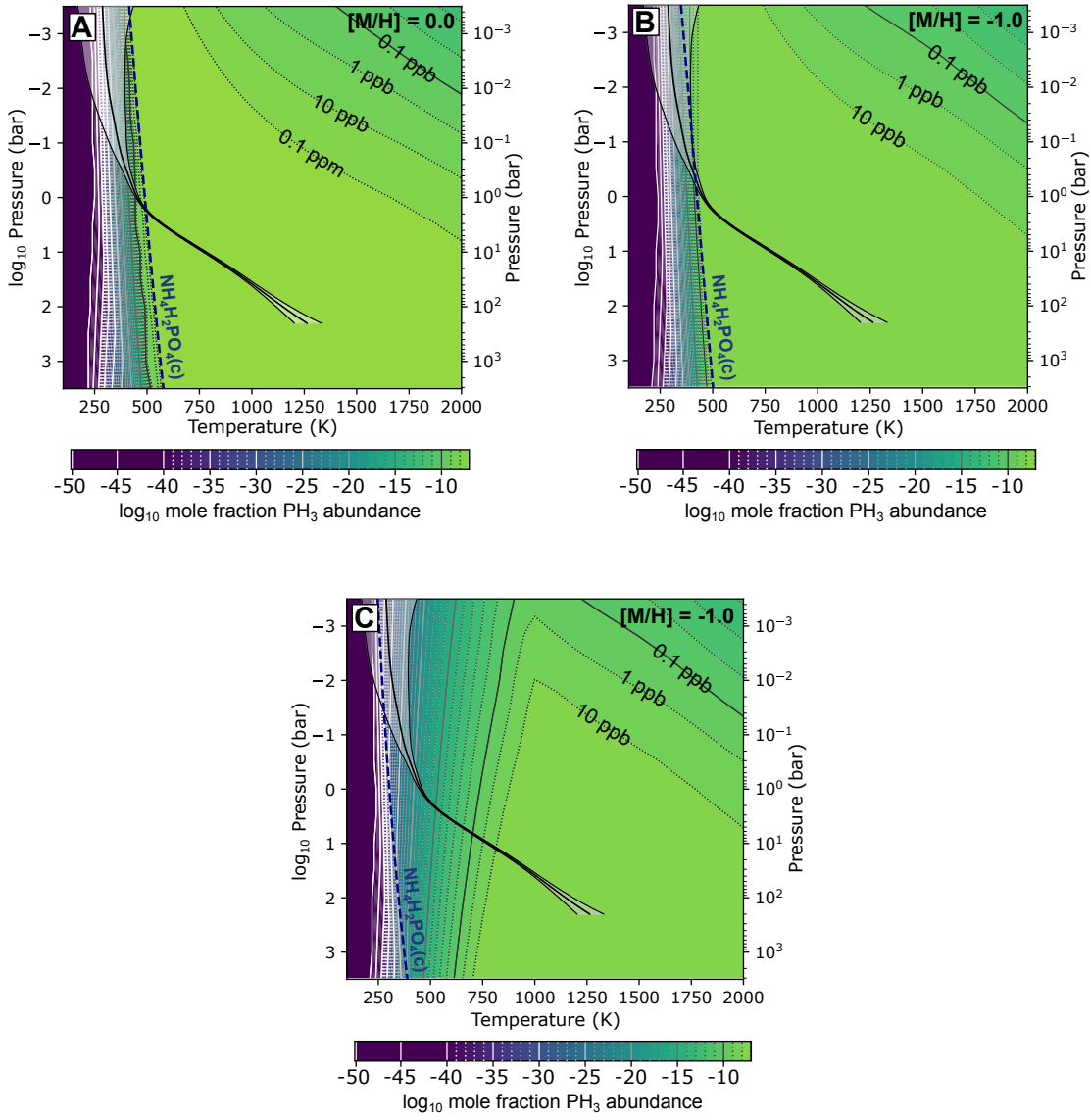


Figure 4: Chemical equilibrium model predictions of PH_3 abundances in the atmosphere of Wolf 1130C. Each panel displays the equilibrium mole fraction abundances for PH_3 in green to purple shading as a function of temperature and pressure. Abundance values are indicated by the associated color bars, and isoabundances are indicated in 1 dex (dotted) and 5 dex (solid) increments (black on green, white on purple), with values between 0.1 ppb (parts per billion) through 0.1 ppm (parts per million) labeled. The near-vertical black dashed line indicates the condensation curve for $\text{NH}_4\text{H}_2\text{PO}_4$, which depletes PH_3 at lower temperatures. The three black curves indicate the median and $\pm 1\sigma$ uncertainty boundaries for the atmospheric thermal profile of Wolf 1130C derived from our retrieval analysis (Fig. S5). (A) A model with solar metallicity and nominal phosphorus chemistry. (B) Same as panel A, but for one tenth of solar metallicity. (C) Same as panel B, but assuming a more exothermic enthalpy of formation for P_4O_6 , leading to depletion of PH_3 at warmer temperatures (35).

References and Notes

1. J. D. Bregman, D. F. Lester, D. M. Rank, Observations of the ν_2 band of PH_3 in the atmosphere of Saturn. *Astrophys. J. Lett.* **202**, L55 (1975), doi:10.1086/181979.
2. S. T. Ridgway, L. Wallace, G. R. Smith, The 800 - 1200 inverse centimeter absorption spectrum of Jupiter. *Astrophys. J.* **207**, 1002–1006 (1976), doi:10.1086/154570.
3. M. Jura, D. G. York, Observations of interstellar chlorine and phosphorus. *Astrophys. J.* **219**, 861–869 (1978), doi:10.1086/155847.
4. M. Agúndez, J. Cernicharo, L. Decin, P. Encrénaz, D. Teyssier, Confirmation of Circumstellar Phosphine. *Astrophys. J. Lett.* **790** (2), L27 (2014), doi:10.1088/2041-8205/790/2/L27.
5. C. Sousa-Silva, *et al.*, Phosphine as a Biosignature Gas in Exoplanet Atmospheres. *Astrobiology* **20** (2), 235–268 (2020), doi:10.1089/ast.2018.1954.
6. E. M. Burbidge, G. R. Burbidge, W. A. Fowler, F. Hoyle, Synthesis of the Elements in Stars. *Rev. Mod. Phys.* **29** (4), 547–650 (1957), doi:10.1103/RevModPhys.29.547.
7. G. Cescutti, F. Matteucci, E. Caffau, P. François, Chemical evolution of the Milky Way: the origin of phosphorus. *Astron. Astrophys.* **540**, A33 (2012), doi:10.1051/0004-6361/201118188.
8. Z. G. Maas, *et al.*, The Galactic Distribution of Phosphorus: A Survey of 163 Disk and Halo Stars. *Astron. J.* **164** (2), 61 (2022), doi:10.3847/1538-3881/ac77f8.
9. M. Asplund, A. M. Amarsi, N. Grevesse, The chemical make-up of the Sun: A 2020 vision. *Astron. Astrophys.* **653**, A141 (2021), doi:10.1051/0004-6361/202140445.
10. I. U. Roederer, H. R. Jacobson, T. Thanathibodee, A. Frebel, E. Toller, Detection of Neutral Phosphorus in the Near-ultraviolet Spectra of Late-type Stars. *Astrophys. J.* **797** (1), 69 (2014), doi:10.1088/0004-637X/797/1/69.
11. E. Caffau, P. Bonifacio, R. Faraggiana, M. Steffen, The Galactic evolution of phosphorus. *Astron. Astrophys.* **532**, A98 (2011), doi:10.1051/0004-6361/201117313.
12. H. R. Jacobson, *et al.*, The Chemical Evolution of Phosphorus. *Astrophys. J. Lett.* **796** (2), L24 (2014), doi:10.1088/2041-8205/796/2/L24.
13. T. Masseron, *et al.*, Phosphorus-rich stars with unusual abundances are challenging theoretical predictions. *Nat. Comm.* **11**, 3759 (2020), doi:10.1038/s41467-020-17649-9.
14. M. Brauner, M. Pignatari, T. Masseron, D. A. García-Hernández, M. Lugaro, Unveiling the chemical fingerprint of phosphorus-rich stars: II. Heavy-element abundances from UVES/VLT spectra. *Astron. Astrophys.* **690**, A262 (2024), doi:10.1051/0004-6361/202451327.
15. K. Bekki, T. Tsujimoto, Phosphorus Enrichment by ONe Novae in the Galaxy. *Astrophys. J. Lett.* **967** (1), L1 (2024), doi:10.3847/2041-8213/ad3fb6.

16. J. Fegley, Bruce, K. Lodders, Atmospheric Chemistry of the Brown Dwarf Gliese 229B: Thermochemical Equilibrium Predictions. *Astrophys. J. Lett.* **472**, L37 (1996), doi:10.1086/310356.
17. C. Visscher, K. Lodders, J. Fegley, Bruce, Atmospheric Chemistry in Giant Planets, Brown Dwarfs, and Low-Mass Dwarf Stars. II. Sulfur and Phosphorus. *Astrophys. J.* **648** (2), 1181–1195 (2006), doi:10.1086/506245.
18. P. Drossart, T. Encrénaz, V. Kunde, R. Hanel, M. Combes, An estimate of the PH₃, CH₃D, and GeH₄ Abundances on Jupiter from the Voyager IRIS data at 4.5 μ m. *Icarus* **49** (3), 416–426 (1982), doi:10.1016/0019-1035(82)90046-X.
19. P. G. J. Irwin, *et al.*, Cloud structure and atmospheric composition of Jupiter retrieved from Galileo near-infrared mapping spectrometer real-time spectra. *J. Geophys. Res.* **103** (E10), 23001–23022 (1998), doi:10.1029/98JE00948.
20. L. N. Fletcher, G. S. Orton, N. A. Teanby, P. G. J. Irwin, Phosphine on Jupiter and Saturn from Cassini/CIRS. *Icarus* **202** (2), 543–564 (2009), doi:10.1016/j.icarus.2009.03.023.
21. A. J. Skemer, *et al.*, The First Spectrum of the Coldest Brown Dwarf. *Astrophys. J. Lett.* **826** (2), L17 (2016), doi:10.3847/2041-8205/826/2/L17.
22. C. V. Morley, *et al.*, An L Band Spectrum of the Coldest Brown Dwarf. *Astrophys. J.* **858** (2), 97 (2018), doi:10.3847/1538-4357/aabe8b.
23. B. E. Miles, *et al.*, Observations of Disequilibrium CO Chemistry in the Coldest Brown Dwarfs. *Astron. J.* **160** (2), 63 (2020), doi:10.3847/1538-3881/ab9114.
24. S. A. Beiler, *et al.*, A Tale of Two Molecules: The Underprediction of CO₂ and Overprediction of PH₃ in Late T and Y Dwarf Atmospheric Models. *Astrophys. J.* **973** (1), 60 (2024), doi:10.3847/1538-4357/ad6759.
25. Z. Rustamkulov, *et al.*, Early Release Science of the exoplanet WASP-39b with JWST NIRSpec PRISM. *Nature* **614** (7949), 659–663 (2023), doi:10.1038/s41586-022-05677-y.
26. L. Welbanks, *et al.*, A high internal heat flux and large core in a warm Neptune exoplanet. *Nature* **630** (8018), 836–840 (2024), doi:10.1038/s41586-024-07514-w.
27. N. L. Wallack, *et al.*, JWST COMPASS: A NIRSpec/G395H Transmission Spectrum of the Sub-Neptune TOI-836c. *Astron. J.* **168** (2), 77 (2024), doi:10.3847/1538-3881/ad3917.
28. M. J. Rowland, *et al.*, Protosolar D-to-H Abundance and One Part per Billion PH₃ in the Coldest Brown Dwarf. *Astrophys. J. Lett.* **977** (2), L49 (2024), doi:10.3847/2041-8213/ad9744.
29. M. Wolf, Einige stärker bewegte Sterne aus der Umgebung der Nova Cygni 3 (1920). *Astron. Nachr.* **213** (2), 31 (1921), doi:10.1002/asna.19212130206.
30. G. N. Mace, *et al.*, The Exemplar T8 Subdwarf Companion of Wolf 1130. *Astrophys. J.* **777** (1), 36 (2013), doi:10.1088/0004-637X/777/1/36.

31. G. N. Mace, *et al.*, Wolf 1130: A Nearby Triple System Containing a Cool, Ultramassive White Dwarf. *Astrophys. J.* **854** (2), 145 (2018), doi:10.3847/1538-4357/aaa8dd.
32. V. M. Woolf, G. Wallerstein, Calibrating M Dwarf Metallicities Using Molecular Indices. *Publ. Astron. Soc. Pac.* **118** (840), 218–226 (2006), doi:10.1086/498459.
33. G. Gilmore, N. Reid, New light on faint stars - III. Galactic structure towards the South Pole and the Galactic thick disc. *Mon. Not. R. Astron. Soc.* **202**, 1025–1047 (1983), doi:10.1093/mnras/202.4.1025.
34. A. J. Burgasser, *et al.*, New Cold Subdwarf Discoveries from Backyard Worlds and a Metallicity Classification System for T Subdwarfs. *Astrophys. J. Lett.* **982** (2), 79 (2025), doi:10.3847/1538-4357/adb39f.
35. Materials and methods are available as supplementary materials.
36. P. Jakobsen, *et al.*, The Near-Infrared Spectrograph (NIRSpec) on the James Webb Space Telescope. I. Overview of the instrument and its capabilities. *Astron. Astrophys.* **661**, A80 (2022), doi:10.1051/0004-6361/202142663.
37. G. S. Wright, *et al.*, The Mid-infrared Instrument for JWST and Its In-flight Performance. *Publ. Astron. Soc. Pac.* **135** (1046), 048003 (2023), doi:10.1088/1538-3873/acbe66.
38. S. A. Beiler, *et al.*, Precise Bolometric Luminosities and Effective Temperatures of 23 Late-T and Y Dwarfs Obtained with JWST. *Astrophys. J.* **973** (2), 107 (2024), doi:10.3847/1538-4357/ad6301.
39. B. Burningham, *et al.*, 76 T dwarfs from the UKIDSS LAS: benchmarks, kinematics and an updated space density. *Mon. Not. R. Astron. Soc.* **433**, 457–497 (2013), doi:10.1093/mnras/stt740.
40. S. Mukherjee, *et al.*, The Sonora Substellar Atmosphere Models. IV. Elf Owl: Atmospheric Mixing and Chemical Disequilibrium with Varying Metallicity and C/O Ratios. *Astrophys. J.* **963** (1), 73 (2024), doi:10.3847/1538-4357/ad18c2.
41. J. Fegley, B., R. G. Prinn, Equilibrium and nonequilibrium chemistry of Saturn's atmosphere - Implications for the observability of PH₃, N₂, CO, and GeH₄. *Astrophys. J.* **299**, 1067–1078 (1985), doi:10.1086/163775.
42. J. Fegley, Bruce, K. Lodders, Chemical Models of the Deep Atmospheres of Jupiter and Saturn. *Icarus* **110** (1), 117–154 (1994), doi:10.1006/icar.1994.1111.
43. C. A. Griffith, R. V. Yelle, Disequilibrium Chemistry in a Brown Dwarf's Atmosphere: Carbon Monoxide in Gliese 229B. *Astrophys. J. Lett.* **519**, L85–L88 (1999), doi:10.1086/312103.
44. D. Saumon, *et al.*, Ammonia as a Tracer of Chemical Equilibrium in the T7.5 Dwarf Gliese 570D. *Astrophys. J.* **647**, 552–557 (2006), doi:10.1086/505419.
45. B. Burningham, *et al.*, Retrieval of atmospheric properties of cloudy L dwarfs. *Mon. Not. R. Astron. Soc.* **470** (1), 1177–1197 (2017), doi:10.1093/mnras/stx1246.

46. E. Gonzales, B. Burningham, Brewster Version Used for Wolf 1130C Science Paper (2025), doi:10.5281/zenodo.17082357, <https://doi.org/10.5281/zenodo.17082357>.

47. K. Lodders, B. Fegley, Atmospheric Chemistry in Giant Planets, Brown Dwarfs, and Low-Mass Dwarf Stars. I. Carbon, Nitrogen, and Oxygen. *Icarus* **155**, 393–424 (2002), doi: 10.1006/icar.2001.6740.

48. K. Hawkins, *et al.*, An accurate and self-consistent chemical abundance catalogue for the APOGEE/Kepler sample. *Astron. Astrophys.* **594**, A43 (2016), doi:10.1051/0004-6361/201628812.

49. C. Visscher, Mapping Jupiter’s Mischief. *J. Geophys. Res. E: Planets* **125** (8), e06526 (2020), doi:10.1029/2020JE006526.

50. P. Ventura, R. Carini, F. D’Antona, A deep insight into the Mg-Al-Si nucleosynthesis in massive asymptotic giant branch and super-asymptotic giant branch stars. *Mon. Not. R. Astron. Soc.* **415** (4), 3865–3871 (2011), doi:10.1111/j.1365-2966.2011.18997.x.

51. P. A. Denissenkov, *et al.*, MESA and NuGrid simulations of classical novae: CO and ONe nova nucleosynthesis. *Mon. Not. R. Astron. Soc.* **442** (3), 2058–2074 (2014), doi:10.1093/mnras/stu1000.

52. M. Wenger, *et al.*, The SIMBAD astronomical database. The CDS reference database for astronomical objects. *Astron. Astrophys. Supp.* **143**, 9–22 (2000), doi:10.1051/aas:2000332.

53. A. Burgasser, *et al.*, JWST/NIRSpec Observations of Wolf 1130C (2025), doi:10.17909/5C42-WC87, <http://archive.stsci.edu/doi/resolve/resolve.html?doi=10.17909/5c42-wc87>.

54. S. Beiler, *et al.*, Models for ”A Tale of Two Molecules: The Underprediction of CO2 and Overprediction of PH3 in Late T and Y Dwarf Atmospheric Models” (2024), doi:10.5281/zenodo.11370830, <https://doi.org/10.5281/zenodo.11370830>.

55. A. Burgasser, aburgasser/ucdmcmc: v1.1 (2025), doi:10.5281/zenodo.16921711, <https://doi.org/10.5281/zenodo.16921711>.

56. H. Bushouse, *et al.*, JWST Calibration Pipeline (2024), doi:10.5281/zenodo.12692459.

57. E. L. Wright, *et al.*, The Wide-field Infrared Survey Explorer (WISE): Mission Description and Initial On-orbit Performance. *Astron. J.* **140**, 1868–1881 (2010), doi:10.1088/0004-6256/140/6/1868.

58. F. Marocco, *et al.*, The CatWISE2020 Catalog. *Astrophys. J. Supp.* **253** (1), 8 (2021), doi: 10.3847/1538-4365/abd805.

59. J. Y. Zhang, *et al.*, Optical constraints on the coldest metal-poor population. *Astron. Astrophys.* **698**, A141 (2025), doi:10.1051/0004-6361/202453246.

60. Gaia Collaboration, *et al.*, Gaia Data Release 3. Summary of the content and survey properties. *Astron. Astrophys.* **674**, A1 (2023), doi:10.1051/0004-6361/202243940.

61. M. Kilic, *et al.*, The Ages of the Thin Disk, Thick Disk, and the Halo from Nearby White Dwarfs. *Astrophys. J.* **837** (2), 162 (2017), doi:10.3847/1538-4357/aa62a5.
62. S. Sharma, *et al.*, The K2-HERMES Survey: age and metallicity of the thick disc. *Mon. Not. R. Astron. Soc.* **490** (4), 5335–5352 (2019), doi:10.1093/mnras/stz2861.
63. M. S. Marley, *et al.*, The Sonora Brown Dwarf Atmosphere and Evolution Models. I. Model Description and Application to Cloudless Atmospheres in Rainout Chemical Equilibrium. *Astrophys. J.* **920** (2), 85 (2021), doi:10.3847/1538-4357/ac141d.
64. K. Lodders, Solar System Abundances and Condensation Temperatures of the Elements. *Astrophys. J.* **591** (2), 1220–1247 (2003), doi:10.1086/375492.
65. N. Metropolis, A. W. Rosenbluth, M. N. Rosenbluth, A. H. Teller, E. Teller, Equation of State Calculations by Fast Computing Machines. *J. Chem. Phys.* **21**, 1087–1092 (1953), doi:10.1063/1.1699114.
66. W. K. Hastings, Monte Carlo sampling methods using Markov chains and their applications. *Biometrika* **57** (1), 97–109 (1970), doi:10.1093/biomet/57.1.97, <http://biomet.oxfordjournals.org/content/57/1/97.abstract>.
67. M. C. Cushing, *et al.*, Atmospheric Parameters of Field L and T Dwarfs. *Astrophys. J.* **678**, 1372–1395 (2008), doi:10.1086/526489.
68. S. Mukherjee, N. E. Batalha, J. J. Fortney, M. S. Marley, PICASO 3.0: A One-dimensional Climate Model for Giant Planets and Brown Dwarfs. *Astrophys. J.* **942** (2), 71 (2023), doi:10.3847/1538-4357/ac9f48.
69. G. Schwarz, Estimating the Dimension of a Model. *Ann. Stat.* **6** (2), 461 – 464 (1978), doi:10.1214/aos/1176344136, <https://doi.org/10.1214/aos/1176344136>.
70. R. E. Kass, A. E. Raftery, Bayes Factors. *J. Am. Stat. Assoc.* **90** (430), 773–795 (1995), doi:10.1080/01621459.1995.10476572, <http://www.tandfonline.com/doi/abs/10.1080/01621459.1995.10476572>.
71. B. Burningham, *et al.*, Cloud busting: enstatite and quartz clouds in the atmosphere of 2M2224-0158. *Mon. Not. R. Astron. Soc.* **506** (2), 1944–1961 (2021), doi:10.1093/mnras/stab1361.
72. E. C. Gonzales, *et al.*, The First Retrieval of a Substellar Subdwarf: A Cloud-free SDSS J125637.13-022452.4. *Astrophys. J.* **923** (1), 19 (2021), doi:10.3847/1538-4357/ac294e.
73. J. K. Faherty, *et al.*, Methane emission from a cool brown dwarf. *Nature* **628** (8008), 511–514 (2024), doi:10.1038/s41586-024-07190-w.
74. D. Foreman-Mackey, D. W. Hogg, D. Lang, J. Goodman, emcee: The MCMC Hammer. *Publ. Astron. Soc. Pac.* **125**, 306–312 (2013), doi:10.1086/670067.
75. O. L. Polyansky, *et al.*, ExoMol molecular line lists XXX: a complete high-accuracy line list for water. *Mon. Not. R. Astron. Soc.* **480** (2), 2597–2608 (2018), doi:10.1093/mnras/sty1877.

76. R. J. Hargreaves, *et al.*, An Accurate, Extensive, and Practical Line List of Methane for the HITEMP Database. *Astrophys. J. Supp.* **247** (2), 55 (2020), doi:10.3847/1538-4365/ab7a1a.

77. L. S. Rothman, *et al.*, HITEMP, the high-temperature molecular spectroscopic database. *J. Quant. Spectrosc. Radiat. Transf.* **111**, 2139–2150 (2010), doi:10.1016/j.jqsrt.2010.05.001.

78. G. Li, *et al.*, Rovibrational Line Lists for Nine Isotopologues of the CO Molecule in the X $^1\Sigma^+$ Ground Electronic State. *Astrophys. J. Supp.* **216** (1), 15 (2015), doi:10.1088/0067-0049/216/1/15.

79. X. Huang, R. R. Gamache, R. S. Freedman, D. W. Schwenke, T. J. Lee, Reliable infrared line lists for 13 CO₂ isotopologues up to E=18,000 cm⁻¹ and 1500 K, with line shape parameters. *J. Quant. Spectrosc. Radiat. Transf.* **147**, 134–144 (2014), doi:10.1016/j.jqsrt.2014.05.015.

80. S. N. Yurchenko, R. J. Barber, J. Tennyson, A variationally computed line list for hot NH₃. *Mon. Not. R. Astron. Soc.* **413** (3), 1828–1834 (2011), doi:10.1111/j.1365-2966.2011.18261.x.

81. D. Saumon, M. S. Marley, M. Abel, L. Frommhold, R. S. Freedman, New H₂ Collision-induced Absorption and NH₃ Opacity and the Spectra of the Coolest Brown Dwarfs. *Astrophys. J.* **750** (1), 74 (2012), doi:10.1088/0004-637X/750/1/74.

82. A. A. A. Azzam, J. Tennyson, S. N. Yurchenko, O. V. Naumenko, ExoMol molecular line lists – XVI. The rotation–vibration spectrum of hot H₂S. *Monthly Notices of the Royal Astronomical Society* **460** (4), 4063–4074 (2016), doi:10.1093/mnras/stw1133, <https://doi.org/10.1093/mnras/stw1133>.

83. C. Sousa-Silva, A. F. Al-Refaie, J. Tennyson, S. N. Yurchenko, ExoMol line lists – VII. The rotation–vibration spectrum of phosphine up to 1500 K. *Monthly Notices of the Royal Astronomical Society* **446** (3), 2337–2347 (2014), doi:10.1093/mnras/stu2246, <https://doi.org/10.1093/mnras/stu2246>.

84. R. S. Freedman, M. S. Marley, K. Lodders, Line and Mean Opacities for Ultracool Dwarfs and Extrasolar Planets. *Astrophys. J. Supp.* **174** (2), 504–513 (2008), doi:10.1086/521793.

85. R. S. Freedman, *et al.*, Gaseous Mean Opacities for Giant Planet and Ultracool Dwarf Atmospheres over a Range of Metallicities and Temperatures. *Astrophys. J. Supp.* **214** (2), 25 (2014), doi:10.1088/0067-0049/214/2/25.

86. N. F. Allard, F. Spiegelman, J. F. Kielkopf, Study of the K-H₂ quasi-molecular line satellite in the potassium resonance line. *Astron. Astrophys.* **465** (3), 1085–1091 (2007), doi:10.1051/0004-6361:20066616.

87. N. F. Allard, J. F. Kielkopf, F. Allard, Impact broadening of alkali lines in brown dwarfs. *Eur. Phys. J. D* **44** (3), 507–514 (2007), doi:10.1140/epjd/e2007-00230-6.

88. J. S. Jenkins, *et al.*, Rotational Velocities for M Dwarfs. *Astrophys. J.* **704** (2), 975–988 (2009), doi:10.1088/0004-637X/704/2/975.

89. C. J. Akerman, L. Carigi, P. E. Nissen, M. Pettini, M. Asplund, The evolution of the C/O ratio in metal-poor halo stars. *Astron. Astrophys.* **414**, 931–942 (2004), doi:10.1051/0004-6361:20034188.

90. S. Borunov, *et al.*, Phosphorus Chemistry in the Atmosphere of Jupiter: A Reassessment. *Icarus* **113** (2), 460–464 (1995), doi:10.1006/icar.1995.1036.

91. D. Wang, J. I. Lunine, O. Mousis, Modeling the disequilibrium species for Jupiter and Saturn: Implications for Juno and Saturn entry probe. *Icarus* **276**, 21–38 (2016), doi:10.1016/j.icarus.2016.04.027.

92. W. Bains, *et al.*, Large Uncertainties in the Thermodynamics of Phosphorus (III) Oxide (P_4O_6) Have Significant Implications for Phosphorus Species in Planetary Atmospheres. *ACS Earth Space Chem.* **7** (6), 1219–1226 (2023), doi:10.1021/acsearthspacechem.3c00016.

93. E. K. H. Lee, *et al.*, A Photochemical Phosphorus-Hydrogen-Oxygen Network for Hydrogen-dominated Exoplanet Atmospheres. *Astrophys. J.* **976** (2), 231 (2024), doi:10.3847/1538-4357/ad8915.

94. L. V. Gurvich, I. V. Veits, C. B. Alcock, *Thermodynamics properties of individual substances. Volume 1 - Elements O, H/D, T/, F, Cl, Br, I, He, Ne, Ar, Kr, Xe, Rn, S, N, P, and their compounds. Part 1 - Methods and computation. Part 2 - Tables (4th revised and enlarged edition)* (Hemisphere Publishing Corp., New York) (1989).

95. B. J. McBride, M. J. Zehe, S. D. Gordon, *NASA Glenn Coefficients for Calculating Thermodynamic Properties of Individual Species*, NASA Technical Memorandum 4513, National Aeronautics and Space Administration, Scientific and Technical Information Program (2002).

96. M. Chase, *NIST-JANAF Thermochemical Tables, 4th Edition* (American Institute of Physics) (1998).

97. H. Kothari, *et al.*, Probing the Heights and Depths of Y Dwarf Atmospheres: A Retrieval Analysis of the JWST Spectral Energy Distribution of WISE J035934.06–540154.6. *Astrophys. J.* **971** (2), 121 (2024), doi:10.3847/1538-4357/ad583b.

98. C. E. Hood, *et al.*, High-Precision Atmospheric Constraints for a Cool T Dwarf from JWST Spectroscopy. *arXiv e-prints* arXiv:2402.05345 (2024), doi:10.48550/arXiv.2402.05345.

99. T. Tsuji, I. Yamamura, S. Sorahana, AKARI Observations of Brown Dwarfs. II. CO_2 as Probe of Carbon and Oxygen Abundances in Brown Dwarfs. *Astrophys. J.* **734** (2), 73 (2011), doi:10.1088/0004-637X/734/2/73.

100. A. J. Burgasser, *et al.*, UNCOVER: JWST Spectroscopy of Three Cold Brown Dwarfs at Kiloparsec-scale Distances. *Astrophys. J.* **962** (2), 177 (2024), doi:10.3847/1538-4357/ad206f.

101. B. K. Gibson, Y. Fenner, A. Kiessling, Galactic Chemical Evolution Redux: Atomic Numbers $6 \leq Z \leq 15$. *Nucl. Phys. A* **758**, 259–262 (2005), doi:10.1016/j.nuclphysa.2005.05.044.

102. L. A. Koelemay, K. R. Gold, L. M. Ziurys, Phosphorus-bearing molecules PO and PN at the edge of the Galaxy. *Nature* **623** (7986), 292–295 (2023), doi:10.1038/s41586-023-06616-1.
103. J. José, M. Hernanz, Nucleosynthesis in Classical Novae: CO versus ONe White Dwarfs. *Astrophys. J.* **494** (2), 680–690 (1998), doi:10.1086/305244.
104. G. Nandakumar, *et al.*, The Galactic chemical evolution of phosphorus observed with IGRINS. *Astron. Astrophys.* **668**, A88 (2022), doi:10.1051/0004-6361/202244724.
105. M. Brauner, *et al.*, Unveiling the chemical fingerprint of phosphorus-rich stars. I. In the infrared region of APOGEE-2. *Astron. Astrophys.* **673**, A123 (2023), doi:10.1051/0004-6361/202346048.
106. N. Svendenius, J. Vergès, The P I Spectrum in the Region 1-4 μ m. *Phys. Scr.* **22** (3), 288–293 (1980), doi:10.1088/0031-8949/22/3/011.
107. M. Afşar, *et al.*, Chemical Compositions of Evolved Stars from Near-infrared IGRINS High-resolution Spectra. I. Abundances in Three Red Horizontal Branch Stars. *Astrophys. J.* **865** (1), 44 (2018), doi:10.3847/1538-4357/aada0c.
108. D. Foreman-Mackey, corner.py: Scatterplot matrices in Python. *The Journal of Open Source Software* **1** (2), 24 (2016), doi:10.21105/joss.00024, <https://doi.org/10.21105/joss.00024>.

Acknowledgments

We thank our three anonymous referees for constructive criticism, which greatly improved this article. This work is based on observations made with the NASA/ESA/CSA James Webb Space Telescope. The data were obtained from the Mikulski Archive for Space Telescopes (MAST) operated by the Space Telescope Science Institute (STScI), which is operated by the Association of Universities for Research in Astronomy, Inc., under NASA contract NAS 5-03127 for JWST. These observations are associated with program # GO-4668. We thank Andrew Fox, Greg Sloan, Alaina Henry, and Wilson Joy Skipper at STScI for their assistance in the planning and execution of JWST observations. This publication makes use of data products from the Wide-field Infrared Survey Explorer (WISE), which is a joint project of the University of California, Los Angeles, and the Jet Propulsion Laboratory/California Institute of Technology, funded by NASA. Data from the European Space Agency (ESA) mission Gaia (<https://www.cosmos.esa.int/gaia>) were processed by the Gaia Data Processing and Analysis Consortium (DPAC; <https://www.cosmos.esa.int/web/gaia/dpac/consortium>). Funding for the DPAC has been provided by national institutions, in particular the institutions participating in the Gaia Multilateral Agreement. This research has made use of the SIMBAD database, operated at CDS, Strasbourg, France (52).

Funding: AB, EG, C-CH, and GS acknowledge funding support from NASA/STScI through JWST general observer program GO-4668, under NASA contract NAS 5-03127. AB, EG and CS-S acknowledge funding support from the Heising-Simons Foundation. CS-S acknowledges funding support from the Portuguese Foundation for Science and Technology. BB acknowledges

funding support from UK Research and Innovation Science and Technology Facilities Council, grant number ST/X001091/1. CV acknowledges funding support from NASA/STScI through JWST archival theory program AR-2232.

Author contributions: AB was principal investigator of the JWST observing program, oversaw execution of the observations, conducted atmosphere grid modeling, and led writing of the manuscript. EG led the atmospheric retrieval analysis with contributions from BB and JF. SB contributed to the atmosphere grid modeling. CV led the atmospheric chemistry modeling. GM and ZZ contributed to analysis of the Wolf 1130 system trinary system. CS-S discussed the phosphine opacity and use as a biosignature. NL, SM, RG, AM, MC, AS, GS, CT, CH, and CA contributed to preparing the JWST proposal and the manuscript writing.

Competing interests: There are no competing interests to declare.

Data and materials availability: The JWST data presented are available at the Mikulski Archive for Space Telescopes (<https://mast.stsci.edu/portal/Mashup/Clients/Mast/Portal.html>) under program JWST-GO-4668 for target name Wolf1130B, and as data collection DOI: 10.17909/5c42-wc87 (53). The modified Sonora Elf-Owl models (EOwl+ (24)) presented in Figure 2 are available at DOI:10.5281/zenodo.11370829 (54). BREWSTER code is available at The BREWSTER code is available at <https://github.com/substellar/brewster> and archived on Zenodo (46). The ucdmcmc code is available at <https://github.com/aburgasser/ucdmcmc> and archived on Zenodo (55). Our best-fitting parameters models are listed in Table S2.

Supplementary Materials

Materials and Methods

Supplementary Text

Tables S1 to S2

Figures S1 to S6

References (56-108)

Supplementary Materials for Observation of undepleted phosphine in the atmosphere of a low-temperature brown dwarf

Adam J. Burgasser*, Eileen C. Gonzales, Samuel A. Beiler, Channon Visscher,
Ben Burningham, Gregory N. Mace, Jacqueline K. Faherty, Zenghua Zhang,
Clara Sousa-Silva, Nicolas Lodieu, Stanimir A. Metchev, Aaron Meisner,
Michael Cushing, Adam C. Schneider, Genaro Suarez, Chih-Chun Hsu,
Roman Gerasimov, Christian Aganze, and Christopher A. Theissen

*Corresponding author. Email: aburgasser@ucsd.edu

This PDF file includes:

Materials and Methods

Supplementary Text

Figures S1 to S6

Tables S1 to S2

Materials and Methods

JWST/NIRSpec Observations

Wolf 1130C was observed with JWST/NIRSpec and JWST/MIRI on 2024 Aug 30 as part of program JWST-GO-4668 (53). NIRSpec/Prism data were acquired using the S200A1 0''.2 fixed slit and Clear filter to obtain low-resolution spectra (resolving power $\lambda/\Delta\lambda = 50\text{--}300$) spanning 0.6 to 5.2 μm . Wolf 1130C was acquired with the F110W filter and offset to the slit position, then observed in spectral mode at two spatial nod positions along the slit, with a sub-pixel dither by 0.5 pixels, equivalent to 0''.05. At each nod position we obtained two exposures consisting of 160 sample-up-the-ramp groups with 1.6 seconds integrations per group, for a total exposure time of 997 seconds.

NIRSpec/G395H data were acquired using the S200A1 plus S200A2 slit combination and the F290LP filter to obtain moderate-resolution spectra ($\lambda/\Delta\lambda = 2,000\text{--}3,700$) spanning 2.9 to 5.1 μm . The dual slit enabled coverage of the 3.7 to 3.8 μm gap between NIRSpec's two detectors. Wolf 1130C was observed in two spatial nod positions for each slit, with 50 sample-up-the-ramp groups and 5.5 seconds integrations per group, for a total exposure time of 1099 seconds.

MIRI/LRS data were acquired using the $4''.7 \times 0''.51$ (42.7 \times 4.6 pixel) slit to obtain low-resolution spectra ($\lambda/\Delta\lambda = 40\text{--}160$) spanning 4 to 14 μm . Wolf 1130C was acquired with the F1000W filter and offset to the slit position, then observed in spectral mode at two spatial nod positions along the slit separated by 1''.9. At each slit position, one exposure was obtained consisting of 100 sample-up-the-ramp groups with 2.8 seconds integrations per group and the FASTR1 readout pattern, for a total exposure time of 555 seconds.

Because Wolf 1130C was well-centered in all spectral exposures, we analyzed the standard pipeline data reduction products. The JWST science calibration pipeline version 1.15.1 (56) was used for all data, which applied background, dark current, and bias subtraction; flat field, gain scale, and linearity corrections; bad pixel flagging; count rate extraction; saturation correction; and 1D spectral extraction. The final one-dimensional spectra have median signal-to-noise (S/N) per pixel values of 300 for the NIRSpec/Prism data and 75 for the NIRSpec/G395H data at 4.1 μm , and S/N = 90 for the MIRI/LRS data at 9 μm .

Luminosity and Effective Temperature of Wolf 1130C

The infrared spectrum of Wolf 1130C includes a large proportion of its total flux, allowing us to estimate its bolometric luminosity. We followed previous work (38) to build the spectral energy distribution (SED) by combining the NIRSpec/Prism and NIRSpec/MIRI spectra. The combined spectrum was calibrated to apparent flux densities using a Wide Field Infrared Explorer (WISE (57)) W2 (4.6 μm) magnitude of Wolf 1130C of 15.14 ± 0.02 (Vega mag) based on photometry from the CatWISE2020 catalog (58, 59). We extrapolated the first spectral point at $\lambda = 0.55 \mu\text{m}$ to zero flux at $\lambda = 0$, and extended a Rayleigh-Jeans tail from the last spectral point at $\lambda = 14 \mu\text{m}$ to $\lambda = \infty$. Integrating over this SED yields a bolometric flux $F_{\text{bol}} = (9.940 \pm 0.006) \times 10^{-17} \text{ W m}^{-2}$. The parallax of the primary star Wolf 1130A from Gaia data release 3 (60), 60.30 ± 0.03 mas, determines the distance to the system, which we adopt for Wolf 1130C. This measure yields a bolometric luminosity relative to the Sun of $\log_{10} (L_{\text{bol}}/L_{\odot}) = -6.068 \pm 0.002$. Because there are absorption features redward of 14 μm in the spectra of low-temperature brown dwarfs, we used a previously computed correction to the Rayleigh-Jeans approximation determined from a sample of

brown dwarfs as a function of absolute W2 magnitude,

$$\Delta \log(L_{\text{bol}}) = 0.0238 \times M_{\text{W2}} - 0.3133 \quad (\text{S1})$$

(38), which has an uncertainty of 0.010 dex at $M_{\text{W2}} = 14.04$ mag. Applying this correction yields $\log_{10}(L_{\text{bol}}/L_{\odot}) = -6.047 \pm 0.003$. The age of this system is currently unconstrained, so we assume 8 to 15 Gyr, which is typical for estimates of the Milky Way's thick disk population (61, 62). Using these values as input for the Sonora Bobcat evolutionary models (63) for a solar-scaled metallicity of $[\text{M}/\text{H}] = -0.5$ leads to the prediction of an effective temperature of $T_{\text{eff}} = 621 \pm 9$ K and a radius $R = 0.80 \pm 0.02$ Jupiter radii (R_{Jup}), values that are used to verify our atmosphere model fits.

Spectral Model Fits to Prism Data

We fit models to the absolute flux-calibrated NIRSpec/Prism spectrum using two versions of the Sonora Elf-Owl atmosphere models: the nominal version in which PH_3 is artificially suppressed to account for its absence in observed brown dwarf spectra (hereafter EOwl (40)) and an expanded chemistry version in which PH_3 abundances are determined from vertical mixing (hereafter EOwl+ (24)). For both versions we considered models with effective temperatures $400 \text{ K} \leq T_{\text{eff}} \leq 1000 \text{ K}$, log surface gravities $4.0 \leq \log_{10}(\text{g}/\text{cm s}^{-2}) \leq 5.5$, log solar-scaled metal abundances $-1 \leq [\text{M}/\text{H}] \leq 1$, C/O linear abundance ratios $0.22 \leq \text{C/O} \leq 1.14$ (as compared to a solar C/O abundance ratio of 0.458 (64)) and log vertical mixing diffusion coefficients $2 \leq \log_{10}(\kappa_{zz}/\text{cm}^2 \text{ s}^{-1}) \leq 9$. Model fitting was conducted using the UCDMCMC package version 1.1, which is archived on Zenodo (55). The observed spectrum was calibrated to absolute flux densities F_{λ} (flux per unit wavelength) using an absolute W2 magnitude of 14.04 ± 0.02 (58–60). The observed spectrum and models were interpolated onto a common wavelength scale that accounts for the variable resolution of the NIRSpec/Prism dispersion, and the models were additionally smoothed by 2 pixel-wide Gaussian profile to account for the projected slit width on the detector.

We conducted an initial grid search to find the single best-fitting model in each of the EOwl model sets, then used these parameters to seed a Metropolis-Hastings Markov Chain Monte Carlo (MCMC) fitting algorithm (65, 66). Models were linearly interpolated across the parameter grid using the logarithm of flux densities and logarithmic parameter values. We used a single chain of 5,000 steps and a reduced χ^2 statistic to iterate model parameters:

$$\chi^2_r = \frac{1}{DOF} \sum_{i=1}^N \frac{(O_i - \alpha M_i)^2}{\sigma_i^2}. \quad (\text{S2})$$

Here, DOF is the degrees of freedom, equal to the number of spectral data points ($N = 820$) minus six free fitting parameters; O_i is the observed spectral flux density; σ_i is the observed spectral uncertainties; M_i is the model spectrum; and α is a scaling factor that minimizes χ^2_r (67):

$$\alpha = \frac{\sum_{i=1}^N M_i O_i / \sigma_i^2}{\sum_{i=1}^N M_i^2 / \sigma_i^2}. \quad (\text{S3})$$

The sum was carried out over all spectral bins i that satisfied $O_i/\sigma_i > 2$. Because the models were computed in surface fluxes and the observed spectrum is scaled to absolute fluxes, corresponding

to a distance $d = 10$ pc, the optimal scale factor $\alpha = (R/10 \text{ pc})^2$ provides an estimate of the source radius, $R = 4.316 \times 10^9 \sqrt{\alpha} R_{\text{Jup}}$. Further details of the fitting procedure are described elsewhere (34).

Fig. 2 displays the best-fitting models for the EOwl and EOwl+ grids, while Table S2 and Fig. S1 present the parameters and uncertainties from the EOwl+ grid fit derived from the MCMC posterior distributions. Both versions of the EOwl models reproduce the overall SED of Wolf 1130C across the 1–5 μm band, with $\sim 20\%$ deviations at the 1.0 μm peak shaped by strong H₂O and CH₄ bands, and at the 3 μm peak where the model predicts excess absorption from NH₃. Both models also produce equivalent physical parameters, including a common radius of $R = 0.74^{+0.04}_{-0.02} R_{\text{Jup}}$. These parameters are consistent with theoretical expectations for an old, evolved brown dwarf (63). However, the EOwl+ models provide a better fit to the 4.0 to 4.5 μm region encompassing the observed PH₃ feature. This region is reproduced by assuming vertical mixing of $\log_{10} (\kappa_{zz}/\text{cm}^2 \text{ s}^{-1}) = 6.5^{+1.6}_{-1.9}$. Using an F-test statistic, we find there is no significant difference between the best EOwl and EOwl+ models over the wavelength range 0.8 to 4.0 μm (p-value = 0.15), but a significant improvement in the fit (p-value < 0.001) for the EOwl+ model over the wavelength range 4.0 to 4.4 μm encompassing the PH₃ feature. Based on this analysis, we conclude that PH₃ is present at an abundance that is consistent with predictions from vertical mixing chemistry.

Phosphine and Carbon Dioxide Abundance

The abundances of PH₃ and CO₂ in the atmosphere of Wolf 1130C were determined using the PICASO radiative transfer code (68), following previous work (24). We started from the EOwl+ model grid, with models encompassing effective temperatures $575 \text{ K} \leq T_{\text{eff}} \leq 750 \text{ K}$; log surface gravities $3.25 \leq \log_{10} (g/\text{cm s}^{-2}) \leq 5.5$; log solar-scaled metallicities [M/H] = −1 and 0 dex; C/O linear abundance ratios C/O = 0.5, 1.0, and 2.5 relative to solar; and log vertical mixing diffusion coefficients $\log_{10} (\kappa_{zz}/\text{cm}^2 \text{ s}^{-1}) = 2, 4, 7, \text{ and } 9$. Using the same pressure-temperature profile as the EOwl+ model and holding all other abundances constant, we explored enhancements in the photospheric abundances of PH₃ (45 ppb $\times 0.2, \times 0.5, \times 1, \text{ and } \times 2$) and CO₂ (9.4×10^{-5} ppb $\times 1, \times 100, \times 500, \times 1,000, \times 5,000, \text{ and } \times 10,000$), and compared our grid of models to the NIRSpec/Prism spectrum of Wolf 1130C as above.

For a solar-scaled abundance of [M/H] = −1, we find a best-fitting model of $T_{\text{eff}} = 600 \text{ K}$, $\log_{10} g = 4.5$, $\log_{10} \kappa_{zz} = 7$, and C/O = 0.23 (half solar), with no enhancement in PH₃ or CO₂ (Fig. S2). These physical parameters are consistent with those inferred from our grid model fitting. The differences between CO₂ enhancement values were minimal due to the absence of a clear feature, although we rule out models with enhancements 500 \times or larger based on comparison of χ^2 values through the Bayesian Information Criterion (BIC; (69)), which yields $\Delta BIC \geq 26$ relative to the model with nominal abundances, indicating very strong evidence against this level of enhancement (70). Similarly, a change in PH₃ to lower and higher values yields $\Delta BIC \geq 4,718$ and 81,323, respectively, indicating very strong evidence against these variations. From this analysis, we conclude that both PH₃ and CO₂ abundances in Wolf 1130C are consistent with predictions of vertical mixing models.

Retrieval Modeling

We conducted an atmospheric retrieval analysis of the absolute flux-calibrated NIRSpec/G395H spectrum of Wolf 1130C using the BREWSTER package (45, 71, 72) following previous methods (73) with the following modifications (46). BREWSTER combines an atmospheric forward model

generator with a Bayesian sampler (EMCEE (74)) to infer the best-fitting pressure-temperature (P/T) profile, molecular gas abundances (f_i), global atmosphere physical parameters ($\log_{10} g$, radius), and kinematic parameters (radial and rotational velocities) that reproduce an observed spectrum. The assumed priors for these parameters are summarized in Table S1. The gas molecules considered were H₂O (75), CH₄ (76), CO (77, 78), CO₂ (79), NH₃ (80, 81), H₂S (82), and PH₃ (83), and additional opacities drawn from the literature (77, 84–87). Volume mixing ratios assumed to be vertically constant throughout the photosphere. We did not include cloud opacity in this analysis. We ran 110,000 iterations with 16 walkers per parameter.

Fig. 3 displays the median likelihood spectral model drawn from our posterior probability distributions, which reproduces the observed spectrum ($\chi^2_r = 6$). Fig. S3 displays the parameter distributions for our retrieved gas abundances, $\log_{10} g$, and radial velocity (v_{rad}). For our derived bulk metallicity, C/O ratio, radius, and mass are listed in Table S2 and shown in Figure S3. The parameters are constrained for all the molecules except CO₂, for which the posterior probability distribution shows a peak at a fractional abundance of $\log f_{\text{CO}_2} = -9.5$ but with a long tail toward the lower limit of our priors; we therefore consider a 3σ upper limit of $\log f_{\text{CO}_2} = -9.2$ (0.6 ppb). We ran separate models for Wolf 1130C to test the impact of excluding PH₃, NH₃, and H₂S absorption, using 35,000–65,000 iterations with 16 walkers per parameter. Compared to the nominal model that includes all three molecules, the PH₃-free model had a relative $\Delta BIC = 1,834$, the NH₃-free model had a relative $\Delta BIC = 212$, and the H₂S-free model had a relative $\Delta BIC = 6$, indicating very strong evidence for PH₃ and NH₃ and strong evidence for H₂S based on the criteria of (70). Fig. S4 compares these models to the full model and spectral data in the regions of the molecules' strongest absorption features, which visually confirm the statistical evidence for PH₃ and NH₃.

Assuming the retrieved molecules contain the majority of their respective elements (excluding hydrogen), as motivated by chemical equilibrium models (17, 63), we estimated elemental abundances relative to the Sun (64). For carbon, we used the CH₄ and CO mixing fractions; for oxygen, we used the H₂O and CO mixing fractions, for nitrogen, we used the NH₃ mixing fraction, for sulfur, we used the H₂S mixing fraction, and for phosphorus, we used the PH₃ mixing fraction. The resulting elemental abundances are listed in Table S2. For nitrogen, our abundance estimate is a lower limit because we cannot constrain the disequilibrium abundance of nitrogen locked up in N₂ due to vertical mixing (44). We estimated an overall metal abundance of $[\text{M}/\text{H}] = -0.68 \pm 0.04$ by combining all the elemental abundances excluding nitrogen. We also estimated an alpha element enrichment of $[\alpha/\text{M}] = +0.30 \pm 0.04$ as a weighted average of the oxygen and sulfur abundances. In addition, we estimated C/O = 0.26 ± 0.01 from the relative C and O abundances, significantly lower than the solar ratio of C/O = 0.458 (64). The overall metallicity and alpha enrichment values of Wolf 1130C are consistent with those measured for the atmosphere of the companion star Wolf 1130A (31, 32, 88) and for other metal-poor thick disk stars (89).

From the retrieved $\log_{10} g$ and radius R , the latter derived from the scaling factor $\alpha = (R/d)^2$ (Eqn. S3), we infer the mass of Wolf 1130C to be $M = g R^2 / G = 44^{+6}_{-5} M_{\text{Jup}}$, where G is the universal gravitational constant. This mass is consistent with an old, evolved brown dwarf, as also indicated by the measured luminosity and inferred T_{eff} from our SED analysis. Our retrieved v_{rad} is also consistent with the center of mass motion of the Wolf 1130AB binary system, which has previously been measured as $-33.2 \pm 0.2 \text{ km s}^{-1}$ (31).

Fig. S5A displays the retrieved thermal profile of Wolf 1130C. Above a pressure of ~ 10 bar, this profile is consistent with the thermal profiles of metal-poor, $T_{\text{eff}} = 600 \text{ K}$ atmospheres predicted by the Sonora Bobcat (63) and Elf-Owl (40) models. However, the retrieved profile deviates in

the deep photosphere, becoming colder at a given pressure as compared to the adiabatic profiles assumed for the grid models. This shallower temperature gradient in the retrieved thermal profile could be due to condensation of KCl and ZnS in the deep photosphere. There is no evidence of continuum opacity or element depletion associated with these condensates, so if they are present it would be in the form of optically thin cloud layers. This deviation occurs at depths that are near the limits of where retrieval modeling is sensitive to the thermal profile. The sensitivity range is indicated by the contribution function (Fig. S5B) which maps the pressure layer from which the observed spectrum emerges as a function of wavelength. The deepest layers at ~ 30 bar are probed around the $4 \mu\text{m}$ peak, the region encompassing PH_3 absorption, which is considerably deeper in Wolf 1130C than in solar-metallicity brown dwarfs (73), and consistent with a more transparent atmosphere with less molecular gas opacity. The majority of the observed spectrum emerges from the 1–20 bar pressure region, where our retrieved profile is in good agreement with that predicted by the metal-poor Elf-Owl model grid.

Chemical Abundance Analysis

To explore the role of mixing, elemental abundances, and thermodynamic assumptions on the atmospheric phosphorus and carbon chemistry of Wolf 1130C, we calculated a suite of chemical equilibrium abundances for PH_3 and CO_2 . We followed the approach of previous studies (17, 63), with equilibrium abundances computed over a wide range of pressures and temperatures at select metal abundances ([M/H]) and C/O abundance ratios. Fig. 4 displays the equilibrium abundances for PH_3 for both solar and one-tenth solar metal abundances and assuming C/O = 0.3. We also show the retrieved thermal profile for Wolf 1130C in this pressure-temperature space. These calculations confirm prior studies that predict PH_3 contains the bulk of the phosphorus reservoir in the photospheres of cool brown dwarfs in equilibrium conditions (17). In the metal-poor case of Wolf 1130C, our model predicts a mixing fraction of 50 ppm along the thermal profile at pressures of 5–20 bar.

In these models, PH_3 remains the dominant phosphorus-bearing gas until it is removed by oxidation and/or condensation at low temperatures. The chemical products of those processes remain poorly constrained due to uncertainties in the enthalpies of formation of oxides such as P_4O_6 (90–93). Different oxide phases have been considered in the literature, including P_4O_6 , P_4O_{10} , and H_3PO_4 gases, and the condensate $\text{NH}_4\text{H}_2\text{PO}_4$ (17, 42, 90, 91). To explore uncertainties in phosphorus chemistry, we calculated equilibrium abundances for two sets of enthalpy data for P_4O_6 : a nominal chemistry (94, 95) in which PH_3 is replaced by H_3PO_4 vapor and then removed by $\text{NH}_4\text{H}_2\text{PO}_4$ condensation at $T_{\text{eff}} \approx 500$ K (49, 91, 92); and a modified chemistry based on P_4O_6 thermodynamic data from the Joint Army-Navy-Air Force (JANAF) thermodynamic tables (96) in which PH_3 is replaced first by P_4O_6 followed by condensation into $\text{NH}_4\text{H}_2\text{PO}_4$ (17). These two scenarios are illustrated in Fig. 4, and indicate that – in the case of chemical equilibrium – the nominal chemistry retains PH_3 in the photosphere of Wolf 1130C, whereas the modified chemistry results in a depletion of PH_3 to ppb levels, which is consistent with measurements and upper limits for other brown dwarfs and gas giant exoplanets (24, 28, 97, 98). Hence, while a change in P_4O_6 thermodynamic quantities could explain the depletion of PH_3 in other low temperature atmospheres, it does not explain the abundance of PH_3 in the atmospheres of Wolf 1130C, Jupiter, or Saturn. In either case, vertical mixing of PH_3 from deep in the atmosphere (where it is most abundant) rules out variations in equilibrium chemistry as an explanation for this molecule’s depletion. The abundant

PH_3 in the atmosphere of Wolf 1130C is compatible with predictions of nominal chemistry models if they also include vertical mixing. It remains unclear why PH_3 has such a low abundance in other brown dwarf and giant exoplanet atmospheres.

We also calculated the equilibrium abundance of CO_2 using the same chemical models, with the results shown in Fig. S6. This model predicts that CH_4 is the dominant carbon-bearing gas throughout the photosphere of Wolf 1130C, with CO_2 abundances decreasing toward lower temperatures as indicated in the Figure, relative to the CH_4 - CO equal-abundance boundary. The model CO_2 abundance is highly sensitive to the C/O ratio and the overall metallicity of the atmosphere (40, 99). While a low value of C/O (as inferred for Wolf 1130C) favors CO_2 formation, the low overall metallicity strongly reduces the CO_2 abundance. Our equilibrium models predict undetectable mixing ratios of 10^{-14} to 10^{-20} across the photosphere of Wolf 1130C. However, CO_2 is also vertically mixed, yielding abundances much higher than the predictions of equilibrium models in low-temperature atmospheres (24, 99). Our analysis suggests that for Wolf 1130C such mixing is insufficient to raise the photospheric CO_2 abundance enough to produce the typically prominent ν_2 feature at 4.3 μm . Metallicity effects on PH_3 and CO_2 abundances imply a $\sim 100\times$ increase in the PH_3/CO_2 abundance ratio relative to solar elemental abundances regardless of vertical mixing (99, 100).

Supplementary Text

Phosphorus in the Spectrum of Wolf 1130A

As discussed in the main text, the phosphorus in the atmosphere of Wolf 1130C could originate in mass transferred from the Wolf 1130B progenitor (13, 50, 101, 102) or ongoing accretion-driven nucleosynthesis (15, 51, 103). Any mass transfer would leave a stronger imprint on the spectrum of the closer Wolf 1130A primary star as compared to Wolf 1130C. While the atmosphere of Wolf 1130A is too warm for PH_3 formation ($T_{\text{eff}} = 3530 \pm 60$ K (31)), atomic phosphorus is found in the near-infrared spectra of metal-poor phosphorus-rich M giants with comparable temperatures (104, 105). We examined previously-acquired high resolution ($\lambda/\Delta\lambda = 45,000$) near-infrared spectral data for Wolf 1130A (31). The spectrum has a signal-to-noise of 500–1,000 around the 1.57115 μm and 1.63829 μm P I lines (104, 106, 107). We find no evidence of P I absorption and set 5σ upper limits on the equivalent widths of 7 mA and 2 mA, respectively. We conclude there is no evidence for phosphorus-rich mass transfer from Wolf 1130B to Wolf 1130A, so no reason to expect it occurred for Wolf 1130C.

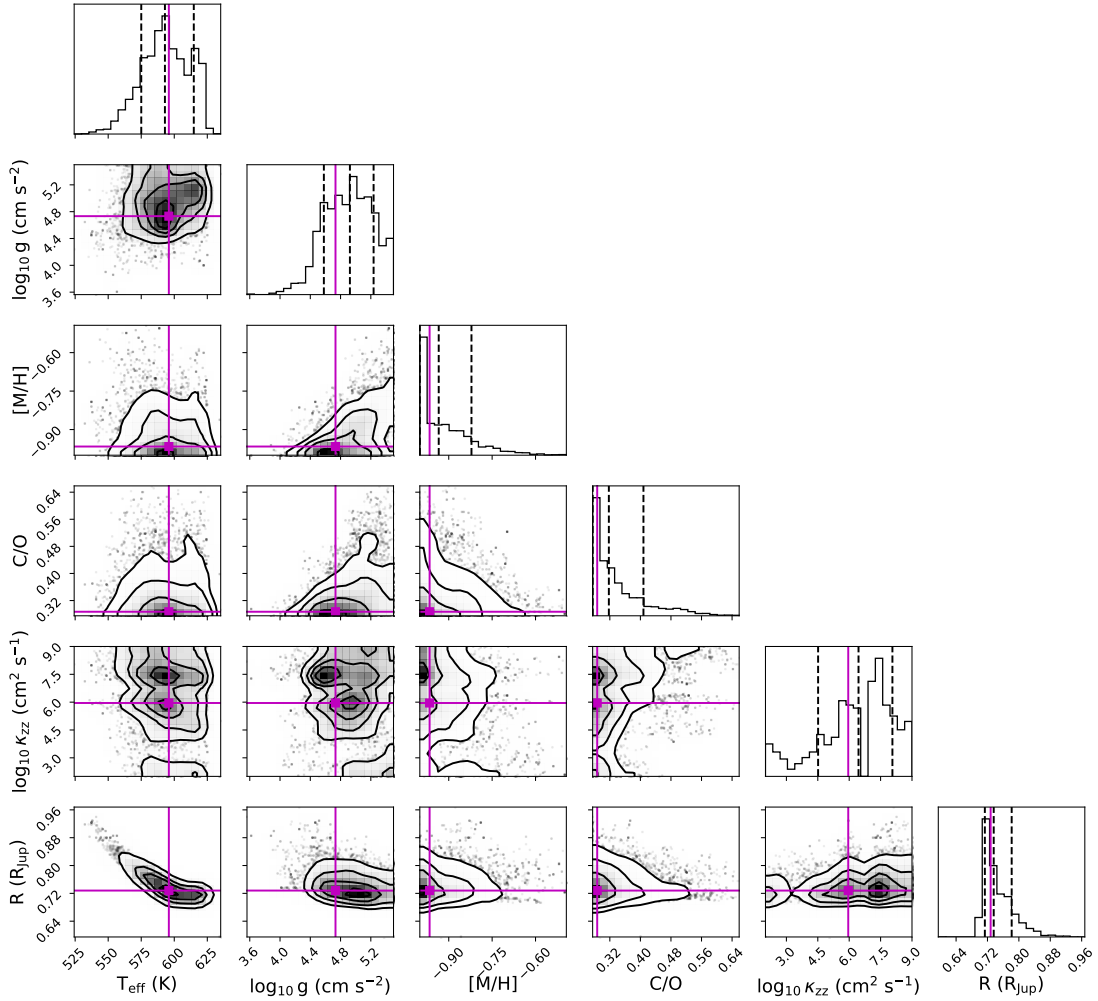


Figure S1: Posterior probability distributions for Sonora Elf-Owl models fitted to the spectrum of Wolf 1130C. Results are shown for fits based on models with PH_3 abundances set by vertical mixing (EOwl+ (24)). Panels along the diagonal show histograms of the marginalized posterior distributions for model parameters T_{eff} , $\log_{10} g$, $[\text{M}/\text{H}]$, C/O , $\log \kappa_{zz}$, and radius R . Off-diagonal panels display the marginalized posterior distributions among parameter pairs as contour plots, with contours set at 25%, 50% and 75% confidence intervals. Solid magenta lines in the posterior distributions indicate the best-fitting value of each parameter, while dashed black lines in the diagonal panels indicate quantiles of 16%, 50% and 84% of the posterior distributions, listed in Table S2. This figure was generated using the CORNER.PY package (108).

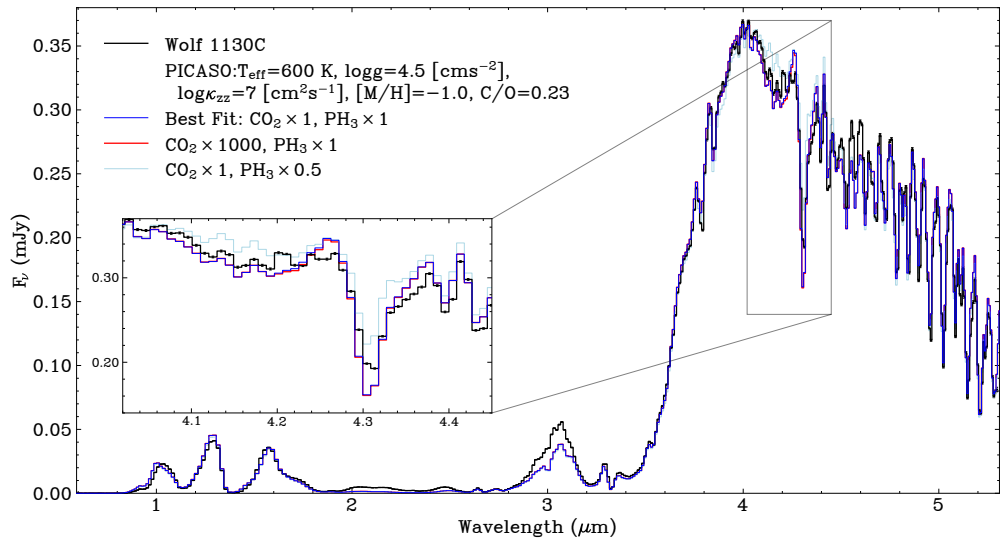


Figure S2: PH_3 and CO_2 abundance analysis for Wolf 1130C. The NIRSpec/Prism spectrum of Wolf 1130C (black line (53)) is compared to three PICASO models with $T_{\text{eff}} = 600$ K, $\log_{10} (\text{g}/\text{cm s}^{-2}) = 4.5$, $\log_{10} (\kappa_{zz}/\text{cm}^2 \text{ s}^{-1}) = 7$, $[\text{M}/\text{H}] = -1.0$, and $\text{C}/\text{O} = 0.23$. The blue line shows the best-fitting model with vertical mixing; the nearly identical red line shows the best-fitting model with 1,000 \times enhancement in CO_2 and no change in PH_3 ; the light blue line shows 0.5 \times reduction in PH_3 and no change in CO_2 . The inset box zooms into the region around the 4.1 μm PH_3 feature to illustrate the differences between those models.

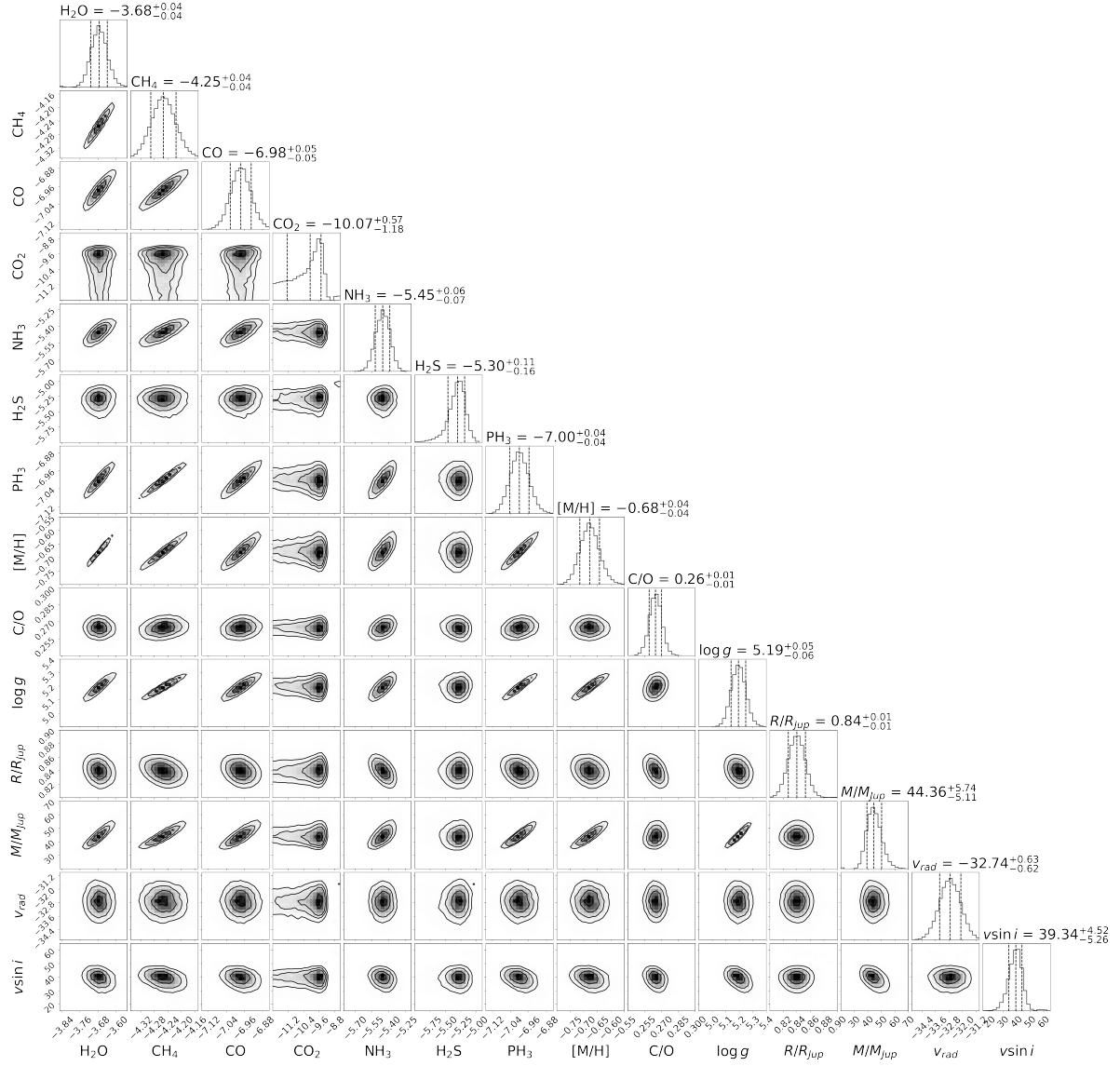


Figure S3: Posterior probability distributions for atmospheric retrieval analysis. Panels along the diagonal show histograms of the marginalized posterior distributions for the model parameters; while off-diagonal panels display the marginalized posterior distributions among parameter pairs as contour plots, indicating correlations between parameters. The dashed lines in the histograms indicate the 16%, 50%, and 84% quantiles for the marginalized distributions. Gas abundances are displayed on a logarithmic scale ($\log_{10} f_i$). $[M/H]$, C/O , radius, and mass are not directly retrieved parameters, but are inferred using the gas abundances, flux scaling factor α , and $\log_{10} g$.

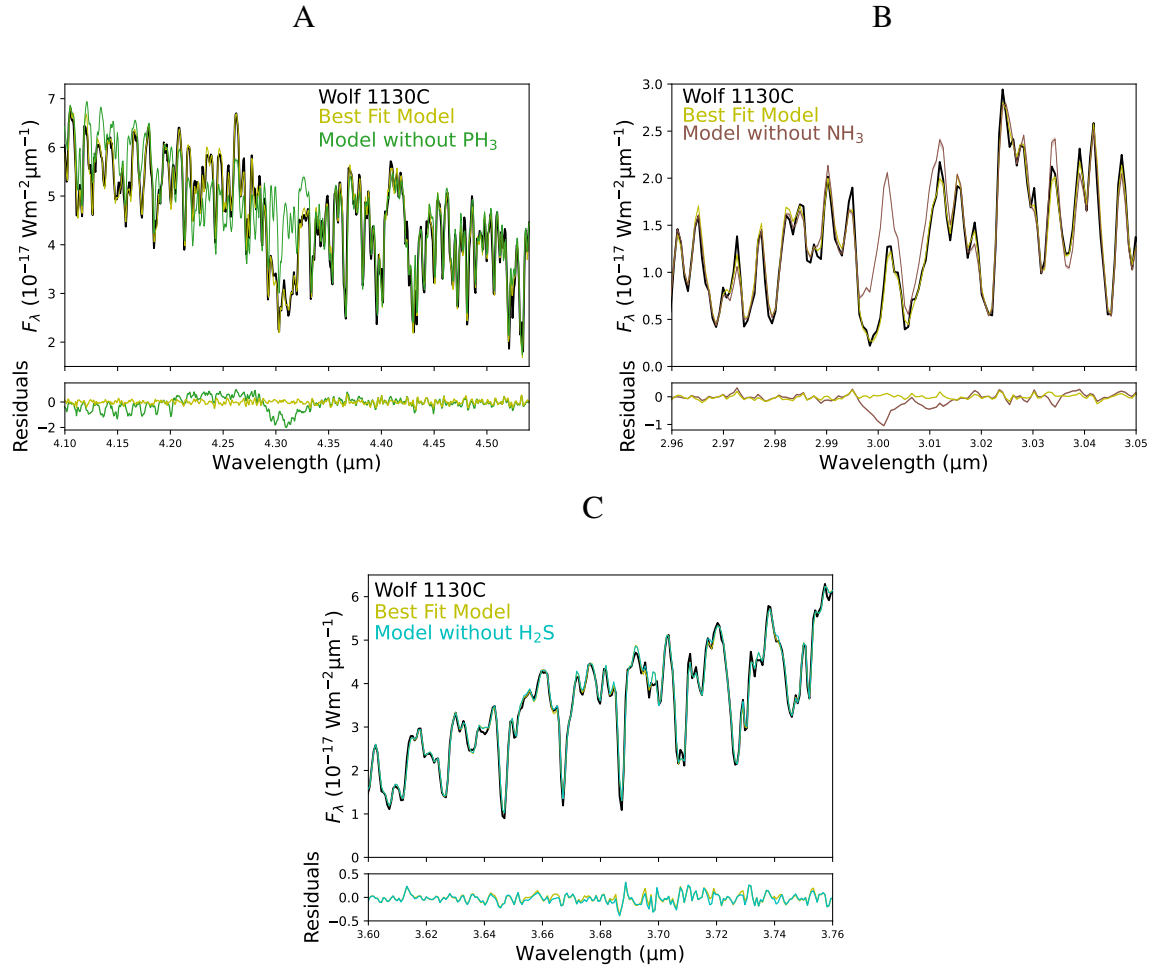


Figure S4: PH₃, NH₃, and H₂S in the atmosphere of Wolf 1130C. Each panel shows close-up views of the NIRSpec/G395H spectrum (black line (53)), the median retrieved model (mustard line), and the median retrieved model without PH₃ (panel A, green line), NH₃ (panel B, brown line), and H₂S (panel C cyan line). At the bottom of each panel is the difference between the observed spectrum and the median retrieved model (mustard line) and models with removed molecules (other colored lines). The Q branches of the $\nu_1 + \nu_3$ stretch modes of PH₃ and NH₃ are visible at 4.3 μm and 3.0 μm , respectively. H₂S features in the 3.65 to 3.75 μm region are not discernible in this visual analysis, but its presence is strongly indicated from our retrieval analysis.

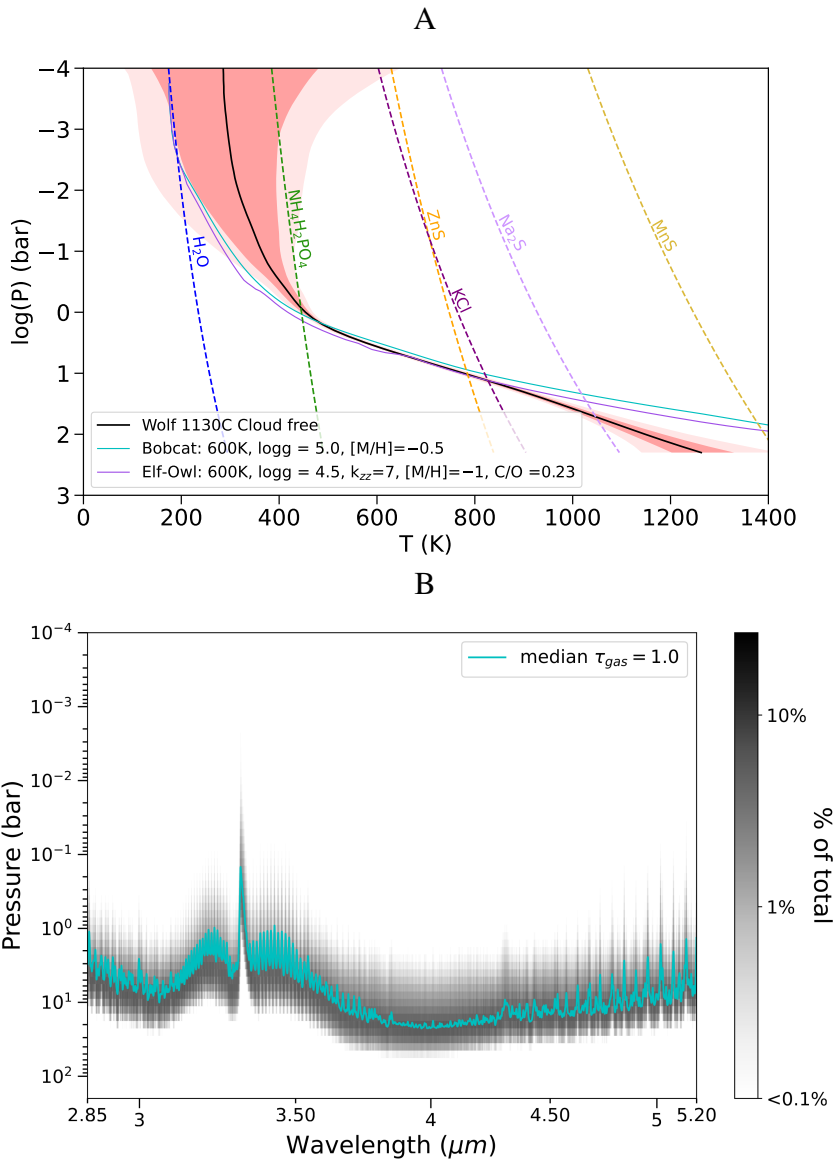


Figure S5: The retrieved thermal profile and contribution function for Wolf 1130C. (A) The median thermal profile from our retrieval analysis (black line), with ± 1 and ± 2 sigma confidence intervals (dark and light salmon shading), respectively. Overlaid are predicted model pressure/temperature profiles from Sonora Bobcat (blue line) and Elf-Owl (purple line) models for the parameters listed in the legend. Dashed lines are the condensation curves at $[M/H] = -0.68$ for H_2O , $NH_4H_2PO_4$, ZnS , KCl , Na_2S , and MnS as labeled. (B) The contribution function to the retrieved spectrum of Wolf 1130C at each wavelength (black shaded region). The median pressure level at a gas optical depth of $\tau_{gas} = 1$ is overplotted (aqua line). The spike and broad feature near $3.3 \mu m$ arises from CH_4 absorption. The bulk of emission emerges from the 1–20 bar pressure region.

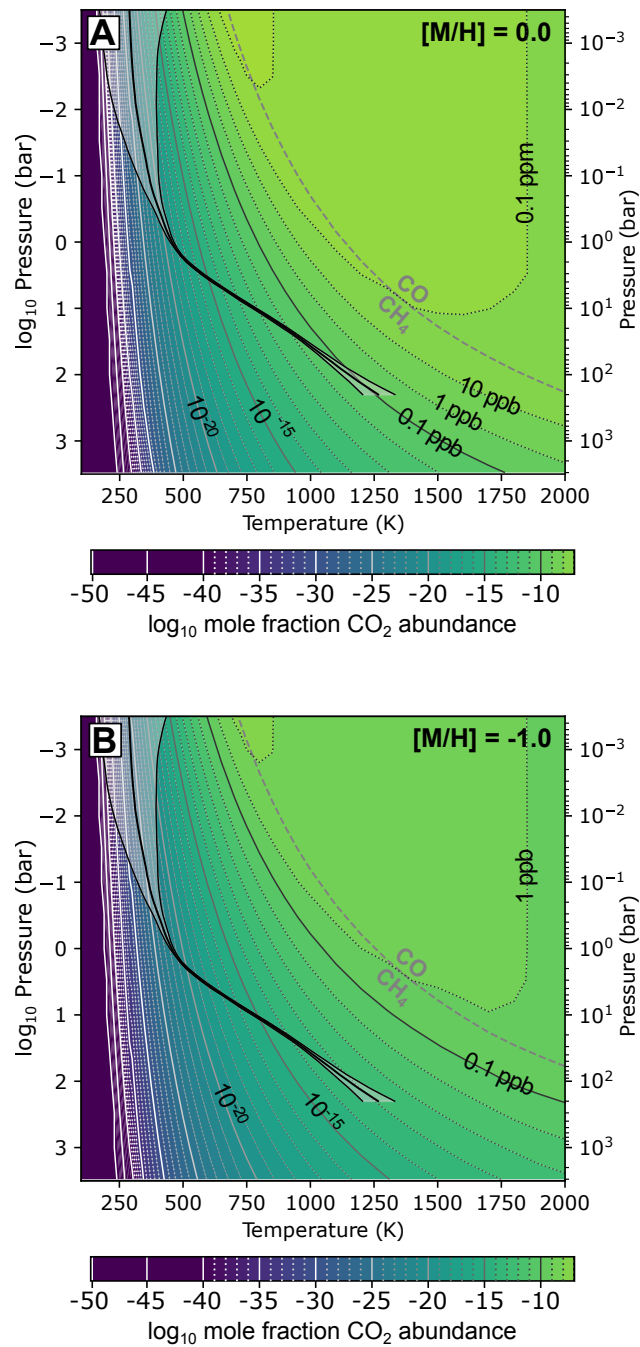


Figure S6: Chemical equilibrium abundances of CO₂ in the atmosphere of Wolf 1130C. Same as Fig. 4 but for CO₂. (A) Results for gas mixtures with C/O = 0.3 and solar metal abundances ([M/H] = 0). (B) Results for one-tenth solar metal abundances ([M/H] = -1). Abundance values are indicated by the color bar, with isoabundance lines indicated in 1 dex (dotted) and 5 dex (solid) increments (black on green, white on purple) and labeled at select intervals. The grey dashed line indicates the equal abundance curve for the primary carbon-bearing species CO and CH₄

Table S1: Parameters and priors for the retrieval analysis. The first column provides a descriptor for each retrieval parameter, the second column shows the corresponding symbol used in the text and Fig. S3, and the third column lists the assumed distribution type and range of the priors. The gas number fractions were fit for molecules H₂O, CH₄, CO, CO₂, NH₃, H₂S and PH₃.

Parameter	Variable	Prior
Gas number fraction	f_i	log-uniform, $\log f_i \geq -12.0$, $\sum_i f_i \leq 1.0$
Thermal profile	$T(P)$	uniform, constrained by $0 \text{ K} < T < 5,000 \text{ K}$
Profile smoothing	γ	uniform, $0 < \gamma < 10^5$
Tolerance factor	b	uniform, $\log(0.01 \times \min(\sigma_i^2)) \leq b \leq \log(100 \times \max(\sigma_i^2))$
Surface gravity	$\log_{10} g$	uniform, constrained by $1 \text{ M}_{\text{Jup}} \leq gR^2/G \leq 80 \text{ M}_{\text{Jup}}$
Scale factor	$\alpha = (R/d)^2$	uniform, assumes $d = 10 \text{ pc}$ and $0.5 \text{ R}_{\text{Jup}} \leq R \leq 2.0 \text{ R}_{\text{Jup}}$
Rotational velocity	$v \sin i$	uniform, $0 \text{ km s}^{-1} < v \sin i < 150 \text{ km s}^{-1}$
Radial velocity	v_{rad}	uniform, $-250 \text{ km s}^{-1} < v_{\text{rad}} < 250 \text{ km s}^{-1}$

Table S2: Derived atmosphere parameters and abundances for Wolf 1130C. The top section lists physical parameters inferred from the SED fitting analysis. The second section lists physical parameters inferred from the Sonora Elf Owl models with PH₃ abundances set by vertical mixing (EOwl+ (24)) fitted to the NIRSpec/Prism spectrum; see Fig. 2. The third section lists physical parameters inferred from our retrieval analysis. The bottom section lists the molecular abundances of H₂O, CH₄, CO, CO₂, NH₃, H₂S and PH₃ inferred from the retrieval analysis, reported as volume mixing ratios assumed to be constant throughout the modeled photosphere; and the derived elemental abundances relative to solar, assuming elements are fully contained in the retrieved molecules. We also list the bulk metallicity [M/H] based on all of the metal abundances excluding nitrogen, the alpha element abundance ratio [α /M] based on the uncertainty-weighted average of [O/M] and [S/M], and the C/O ratio based on the carbon and oxygen abundances. All uncertainties reflect 68% confidence intervals. Upper limit for CO₂ reflects 3 σ limit. Lower limit for [N/M] reflects the unknown abundance of N contained in N₂. Where multiple values are available from different analyses, those marked with a * are our assumed to be fiducial values.

SED Physical Parameters					
Quantity	Value	Unit	Quantity	Value	Unit
log(L _{bol} /L _⊙)	-6.047±0.003	dex	Radius*	0.80±0.02	R _{Jup}
T _{eff} *	621±9	°K			
Grid Model Fit Physical Parameters					
Quantity	Value	Unit	Quantity	Value	Unit
T _{eff}	593 ⁺²¹ ₋₁₈ K	°K	C/O	0.32 ^{+0.09} _{-0.04}	
log ₁₀ g	4.9±0.3	cm s ⁻²	log κ_{zz}	6.5 ^{+1.6} _{-1.9}	cm ² s ⁻¹
[M/H]	-0.93 ^{+0.11} _{-0.07}	dex	Radius	0.74 ^{+0.04} _{-0.02}	R _{Jup}
Retrieved Physical Parameters					
Quantity	Value	Unit	Quantity	Value	Unit
log g*	5.19 ^{+0.05} _{-0.06}	dex	Radius	0.84±0.01	R _{Jup}
v_{rad}	-32.7±0.7	km/s	Mass	44 ⁺⁶ ₋₅	M _{Jup}
Retrieved Abundances					
Species	Log Abundance	Unit	Quantity	Value	Unit
H ₂ O	-3.68 ± 0.04	dex	[C/M]	+0.04 ± 0.06	dex
CH ₄	-4.25 ± 0.04	dex	[O/M]	+0.32 ± 0.06	dex
CO	-6.98 ± 0.05	dex	[N/M]	≥-0.60 ± 0.13	dex
CO ₂	≤ -9.2	dex	[S/M]	+0.19 ^{+0.13} _{-0.16}	dex
NH ₃	-5.45 ^{+0.06} _{-0.07}	dex	[P/M]	+0.22 ± 0.06	dex
H ₂ S	-5.30 ^{+0.11} _{-0.16}	dex	[M/H]*	-0.68 ± 0.04	dex
PH ₃	-7.00 ± 0.04	dex	[α /M]	+0.30 ± 0.04	dex
			C/O*	0.26 ± 0.01	